

# Structure and Instability of the Ionization Fronts around Moving Black Holes

Kazuyuki Sugimura<sup>1</sup><sup>★</sup> and Massimo Ricotti<sup>1</sup><sup>†</sup>

<sup>1</sup>*Department of Astronomy, University of Maryland, College Park, MD 20740, USA*

Accepted XXX. Received YYY; in original form ZZZ

## ABSTRACT

In this paper we focus on understanding the physical processes that lead to stable or unstable ionization fronts (I-fronts) observed in simulations of moving black holes (BHs). The front instability may trigger bursts of gas accretion, rendering the BH significantly more luminous than at steady-state. We perform a series of idealized three dimensional radiation hydrodynamics simulations resolving the I-fronts around BHs of mass  $M_{\text{BH}}$  and velocity  $v_{\infty}$  accreting from a medium of density  $n_{\text{H}}$ . The I-front, with radius  $R_{\text{I}}$ , transitions from D-type to R-type as the BH velocity becomes larger than a critical value  $v_{\text{R}} \sim 40$  km/s. The D-type front is preceded by a bow-shock of thickness  $\Delta R_{\text{I}}$  that decreases as  $v_{\infty}$  approaches  $v_{\text{R}}$ . We find that both D-type and R-type fronts can be unstable given the following two conditions: i) for D-type fronts the shell thickness must be  $\Delta R_{\text{I}}/R_{\text{I}} < 0.05$  (*i.e.*,  $v_{\infty} \gtrsim 20$  km/s.), while no similar restriction holds for R-type fronts; ii) the temperature jump across the I-front must be  $T_{\text{II}}/T_{\text{I}} > 3$ . This second condition is satisfied if  $T_{\text{I}} < 5000$  K or if  $n_{\text{H}} M_{\text{BH}} \gtrsim 10^6 M_{\odot} \text{cm}^{-3}$ . Due to X-ray pre-heating typically  $T_{\text{I}} \sim 10^4$  K, unless the D-type shell is optically thick to X-rays, which also happens when  $n_{\text{H}} M_{\text{BH}}$  is greater than a metallicity-dependent critical value. We thus conclude that I-fronts around BHs are unstable only for relatively massive BHs moving through very dense molecular clouds. We briefly discuss the observational consequences of the X-ray luminosity bursts likely associated with this instability.

**Key words:** accretion, accretion discs – black hole physics – hydrodynamics – instabilities – radiative transfer – methods: numerical.

## 1 INTRODUCTION

After the merger of galaxies hosting intermediate-mass black holes ( $10^2 M_{\odot} \lesssim M_{\text{BH}} \lesssim 10^5 M_{\odot}$ ; IMBHs), the IMBHs are likely to move around the post-merger galaxies while accreting the surrounding gas. The accretion growth of such IMBHs is considered to play a critical role in the stellar-mass BH seed scenario of the formation of supermassive BHs ( $M_{\text{BH}} \gtrsim 10^6 M_{\odot}$ ; SMBHs) that reside at the center of almost all galaxies (see, e.g., Volonteri 2012; Inayoshi et al. 2019, for review). Furthermore, X-ray emission from the accretion disks of IMBHs can build up an X-ray background that may affect the star-formation history of the Universe (e.g., Ricotti 2016). The efficiency of gas accretion, however, is yet to be fully understood because of the reasons described below.

Recently, theoretical works have revealed that various factors can widely change the efficiency of accretion. In the simplest case of a stationary BH emitting isotropic radiation, the formation of the ionized bubble significantly reduces the

accretion rate (Milosavljević et al. 2009a,b; Park & Ricotti 2011, 2012). The reduction, however, is notably weakened if the radiation is anisotropic as a result of the disk shadowing effect (Sugimura et al. 2017; Takeo et al. 2018), or if the surrounding gas is so dense as to confine the ionized bubble to the vicinity of the BH (Inayoshi et al. 2016). Other effects such as the radiation pressure and attenuation by dust grains (Yajima et al. 2017; Toyouchi et al. 2019) and the gas angular momentum (Sugimura et al. 2018) are also critical factors that determine the accretion rate.

For the more realistic case of a BH moving in the surrounding medium (or equivalently a stationary BH in a homogeneously moving medium), the gas accretion under radiative feedback was first studied in Park & Ricotti (2013, hereafter PR13). PR13 performed axisymmetric 2D simulations assuming that gas flows into the computational region from the polar direction of the spherical coordinates. They found that the ionization front (I-front) is D-type and a dense shell forms in front of it in the low-velocity case, but that it becomes R-type and the shell disappears in the high-velocity case. The gravitational attraction by the dense shell can accelerate the BH, preventing it from sinking to the cen-

<sup>★</sup> E-mail: sugimura@astro.umd.edu

<sup>†</sup> E-mail: ricotti@astro.umd.edu

ter of the galaxy by dynamical friction (Park & Bogdanović 2017; Toyouchi et al. 2020). PR13 also found that the accretion rate increases with BH velocity in the regime when the I-front is D-type, contrary to the classical Bondi-Hoyle-Lyttleton (BHL) accretion, for which the accretion rate is a monotonically decreasing function of the velocity. More interestingly, the I-front becomes unstable near the D- and R-type transition, and the instability triggers accretion bursts. The bursty-mode accretion can enhance the BH growth rate. Moreover, even if the mean accretion rate is weakly affected by the accretion bursts, the associated luminosity bursts are significantly brighter than the mean, because the radiative efficiency of BH accretion disk is higher with the higher accretion rate in the so-called radiatively inefficient accretion flow (RIAF) regime (Narayan & Yi 1994).

The axisymmetric 2D simulations in PR13, however, are not suitable for studying the instability of the I-front for two reasons. First, although the instability grows along the polar axis in their simulations, the gas dynamics near the polar axis is likely affected by numerical artifacts because the polar axis is the coordinate singularity of the spherical coordinates. Second, the growth and saturation of the instability is essentially a 3D process, as we will show in this paper, and cannot be followed by the 2D simulations. Therefore, we need to perform new 3D simulations to reveal the true nature of the instability.

3D simulations that resolve the inner scale where the BH gravity dominates the gas dynamics (*i.e.*, the scale of the BHL radius, typically a hundred times smaller than the I-front) can follow the gas accretion taking into account the interplay of the instability and the modulated luminosity. The analysis of such simulations, however, is challenging because of the complicated interactions of various physical processes. Moreover, the wide dynamic range makes the computational cost expensive since we require 3D simulations with high resolution near the BH to resolve feedback effects, and near the I-front to resolve the instability.

Therefore, as a first step toward understanding the BH accretion rate and luminosity modulated by the instability of the I-front, we focus on resolving the region outside the BHL radius by performing a set of 3D radiation hydrodynamics simulations of gas dynamics near the I-front, assuming constant BH luminosity and neglecting the BH gravity (since the I-front radius is much larger than the BHL radius). By extending the analytical model developed in PR13, we provide a physically motivated model for the observed properties of the bow shocks in simulated D-type fronts. We also discuss the conditions for the instability based on the simulation results.

This paper is organized as follows. In Sec. 2, we describe the analytical model. In Sec. 3 and Sec. 4, we describe our 3D radiation hydrodynamics simulations and present the simulation results, respectively. We discuss the implication of our work in Sec. 5 and finally present a summary in Sec. 6.

## 2 ANALYTICAL MODEL OF FLOW AROUND MOVING BH WITH RADIATION FEEDBACK

### 2.1 Park-Ricotti model

Here, we briefly review the analytical model developed in PR13. This quasi-1D model of flow around a moving BH with radiation feedback reproduces the variation of the type of flow and the resulting accretion rate as a function of BH velocity observed in their simulations. We refer the readers to PR13 for the details of this model.

The model considers the structure of flow along the axis of the BH motion. In the BH rest frame, the gas is moving toward the BH with velocity  $v_\infty$ . Hereafter, the subscripts I and II indicate the neutral and ionized sides of the I-front, respectively. For simplicity, we assume that the sound speed (or temperature) discontinuously changes from  $c_I$  in the neutral gas upstream of the I-front to  $c_{II}$  in the ionized gas across the I-front. In this section, we assume that the BH velocity with respect to the neutral ambient gas is supersonic (*i.e.*,  $v_\infty \geq c_\infty$ ), and the ambient gas has constant temperature, *i.e.*,  $c_I = c_\infty$ . We consider the subsonic case ( $v_\infty < c_\infty$ ), as well as the effect of X-ray pre-heating of the ambient gas ( $c_I \neq c_\infty$ ), in Appendix A.

Let us begin with writing down the jump conditions for density  $\rho$  and velocity  $v$  across the I-front,

$$\frac{\rho_{II}}{\rho_I} = \frac{v_I}{v_{II}} = \frac{c_I^2 + v_I^2 \pm \sqrt{(c_I^2 + v_I^2)^2 - 4c_{II}^2 v_I^2}}{2c_{II}^2} \quad \left( \equiv \Delta^{(\pm)}(v_I, c_I, c_{II}) \right). \quad (1)$$

In order for Eq. (1) to have a (real) solution, the condition  $v_I < v_D$  or  $v_I > v_R$  must be satisfied. Here, the D-type critical velocity is defined as

$$v_D(c_I, c_{II}) \equiv c_{II} - \sqrt{c_{II}^2 - c_I^2} \approx \frac{c_I^2}{2c_{II}} \quad (c_I \ll c_{II}), \quad (2)$$

and the R-type critical velocity is

$$v_R(c_I, c_{II}) \equiv c_{II} + \sqrt{c_{II}^2 - c_I^2} \approx 2c_{II} \quad (c_I \ll c_{II}). \quad (3)$$

The I-fronts with  $v_I < v_D$  and  $v_I > v_R$  are called D-type and R-type, respectively.

In the case with  $v_\infty > v_R$ , the gas can directly reach the I-front with  $v_I = v_\infty$  and  $\rho_I = \rho_\infty$ . The I-front becomes weak R-type (*i.e.*, the minus sign is taken in Eq. 1), and the density and velocity inside the HII region are given, respectively, as

$$\rho_{II,R} = \Delta^{(-)}(v_\infty, c_I, c_{II}) \rho_\infty, \quad (4)$$

and

$$v_{II,R} = \frac{1}{\Delta^{(-)}(v_\infty, c_I, c_{II})} v_\infty. \quad (5)$$

Here, the density and velocity jump is generally weak because  $\Delta^{(-)}$  takes its maximum value of 2 ( $c_I \ll c_{II}$ ) at  $v_\infty = v_R$  and approaches unity as  $v_\infty$  increases. Hereafter, we name this type of flows as the R-type flows.

In the case with ( $v_D < c_I <$ )  $v_\infty < v_R$ , however, the jump conditions in Eq. (1) cannot be satisfied without extra structures. In this case, a shock is generated in front of the I-front. The gas experiencing the shock forms a dense shell between

the shock and the I-front. The I-front becomes D-type because the gas slows down to below  $v_D$  as a result of the following two effects. Firstly, the isothermal shock decreases the velocity by  $(v_\infty/c_I)^2$ , while increasing the density by the same factor. Secondly, the tangentially diverging motion decelerates the gas in the shell (we will discuss this process in detail in Sec. 2.2). In PR13, they further assumed that the I-front is critical D-type (*i.e.*,  $v_I = v_D$ ), and thus the velocity inside the HII region is given by

$$v_{II,D} = c_{II}. \quad (6)$$

Here, the total pressure  $P_{\text{tot}} = \rho(v^2 + c_s^2)$ , defined as the sum of the ram pressure  $P_{\text{ram}} = \rho v^2$  and the thermal pressure  $P_{\text{th}} = \rho c_s^2$ , is conserved across the shock and the I-front. It is also conserved inside the shocked shell, where the flow is subsonic, because  $P_{\text{tot}} \approx P_{\text{th}}$  and  $P_{\text{th}}$  is conserved due to the approximate pressure equilibrium. From Eq. (6) and  $P_{\text{tot}} = \rho_\infty(v_\infty^2 + c_I^2)$ , the density inside the HII region is given by

$$\rho_{II,D} = \frac{\rho_\infty(v_\infty^2 + c_I^2)}{2c_{II}^2}. \quad (7)$$

Hereafter, we name this type of flows as the D-type flows.

Using the density and velocity inside the HII region obtained above, the accretion rate can be estimated with the Bondi-Hoyle-Lyttleton (BHL) formula as

$$\dot{M} = \frac{4\pi G^2 M_{\text{BH}}^2 \rho_{II}}{(v_{II}^2 + c_{II}^2)^{3/2}} = \begin{cases} \dot{M}_D & c_I < v_\infty < v_R \\ \dot{M}_R & v_\infty > v_R \end{cases}, \quad (8)$$

where the accretion rate for the D-type flows

$$\dot{M}_D = \frac{\pi G^2 M_{\text{BH}}^2 \rho_\infty (v_\infty^2 + c_I^2)}{\sqrt{2} c_{II}^5} \quad (9)$$

and that for the R-type flows

$$\dot{M}_R = \frac{4\pi G^2 M_{\text{BH}}^2 \rho_\infty \Delta^{(-)}(v_\infty, c_I, c_{II})}{\left(c_{II}^2 + \left(\frac{v_\infty}{\Delta^{(-)}(v_\infty, c_I, c_{II})}\right)^2\right)^{3/2}} \approx \frac{4\pi G^2 M_{\text{BH}}^2 \rho_\infty}{\left(c_{II}^2 + v_\infty^2\right)^{3/2}} \quad (v_\infty \gg v_R). \quad (10)$$

Here, we have used  $\rho_{II}$  and  $v_{II}$  given by Eqs. (4) and (5) for  $\dot{M}_R$  and those given by Eqs. (6) and (7) for  $\dot{M}_D$ . In Fig. 1, we plot the accretion rate given by Eq. (8), with the temperature of the neutral gas  $T_I = 10^4$  K ( $c_I = 8.1$  km/s) and that of the ionized gas  $T_{II} = 4 \times 10^4$  K ( $c_{II} = 23$  km/s). We use the same  $T_I$  and  $T_{II}$  for the Park & Ricotti model in the rest of the paper unless otherwise stated. As pointed out in PR13,  $\dot{M}$  takes its maximum value at  $v_\infty = v_R$  in Figure 1.

For  $\dot{M}$  obtained above, the luminosity of the X-ray emission from the BH accretion disk can be calculated as

$$L = \eta \dot{M} c^2. \quad (11)$$

with radiative efficiency  $\eta$ . Here, we assume an  $\dot{M}$ -dependent efficiency modeled as

$$\eta = \eta_0 \times \min\left(1, \frac{\dot{M} c^2}{L_{\text{Edd}}}\right), \quad (12)$$

with the normalization factor  $\eta_0 = 0.1$ . The Eddington luminosity is defined as  $L_{\text{Edd}} \equiv 4\pi G M_{\text{BH}} c m_p / \sigma_T$ , where  $m_p$  is the proton mass and  $\sigma_T = 6.65 \times 10^{-25}$  cm<sup>2</sup> is the Thomson cross-section. This form of  $\eta$  is motivated by the fact that

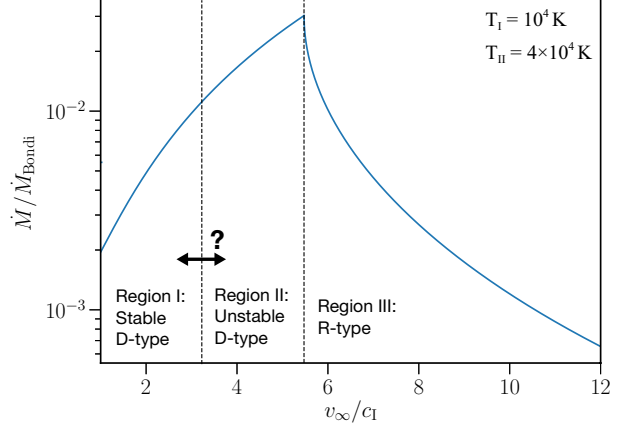


**Figure 1.** The analytical accretion rate from Park & Ricotti model. We plot the accretion rate given by Eq. (8) for a BH moving at velocity  $v_\infty$ , with  $T_I = 10^4$  K and  $T_{II} = 4 \times 10^4$  K. The accretion rate is normalized by the Bondi accretion rate  $\dot{M}_{\text{Bondi}} = 4\pi \lambda_B G^2 M_{\text{BH}}^2 / c_\infty^3$  with  $\lambda_B = 1$ , and thus the dependence on  $M_{\text{BH}}$  and  $\rho_\infty$  is completely canceled out. There are three regions demarcated by the vertical dashed lines: the stable D-type flows (left), the unstable D-type flows (center), and the R-type flows (right). While the transition from the stable D-type to the unstable D-type was seen in the simulations of PR13, the condition for the instability was not clear in PR13.

the radiative efficiency becomes lower with lower  $\dot{M}$  in the low accretion rate RIAF regime (Narayan & Yi 1994).

In order to better understand the stability of the I-front, we estimate its size  $R_{\text{IF}}$ , using the luminosity and density modeled above. As pointed out in PR13,  $R_{\text{IF}}$  is either determined by the balance of the ionization and recombination rates inside the ionized region, or by the balance of the ionization rate and the flow rate of neutral gas across the I-front. In the former case,  $R_{\text{IF}}$  is well approximated by the Strömgen radius,

$$r_{\text{Strm}} \equiv \left(\frac{3\dot{N}_{\text{ion}}}{4\pi n_{\text{II}}^2 \alpha_B}\right)^{1/3}, \quad (13)$$

where  $\dot{N}_{\text{ion}} = L/\langle h\nu \rangle$  is the ionizing photon emission rate, with average energy of ionizing photons  $\langle h\nu \rangle$ ,  $n_{\text{II}} \approx \rho_{\text{II}}/m_p$  is the ionized gas number density, and  $\alpha_B \approx 8.3 \times 10^{-14}$  cm<sup>3</sup> s<sup>-1</sup> ( $T_{\text{II}}/4 \times 10^4$  K)<sup>-1</sup> is the Case-B recombination coefficient (Ferland et al. 1992). Alternatively, in the latter case,  $R_{\text{IF}}$  is approximated by

$$r_{\text{neutral-flow}} \equiv \left(\frac{\dot{N}_{\text{ion}}}{4\pi n_{\text{II}} v_{\text{II}}}\right)^{1/2}, \quad (14)$$

where we have used the particle number conservation  $n_{\text{I}} v_{\text{I}} = n_{\text{II}} v_{\text{II}}$  across the I-front. The size  $R_{\text{IF}}$  is determined by the smaller between  $r_{\text{Strm}}$  and  $r_{\text{neutral-flow}}$ . For the cases explored in our simulations, generally we have  $r_{\text{Strm}} \leq r_{\text{neutral-flow}}$ , and thus  $R_{\text{IF}} \sim r_{\text{Strm}}$ .

In the RIAF regime ( $\dot{M} < L_{\text{Edd}}/c^2$ ; see Eq. 12), with Eqs. (5), (11), (13), and (14), we can show that the condition  $r_{\text{Strm}} > r_{\text{neutral-flow}}$  is satisfied if

$$v_\infty \gtrsim (80 \text{ km/s}) \left(\frac{n_\infty M_{\text{BH}}}{10^6 M_\odot \text{ cm}^{-3}}\right)^{1/3}. \quad (15)$$

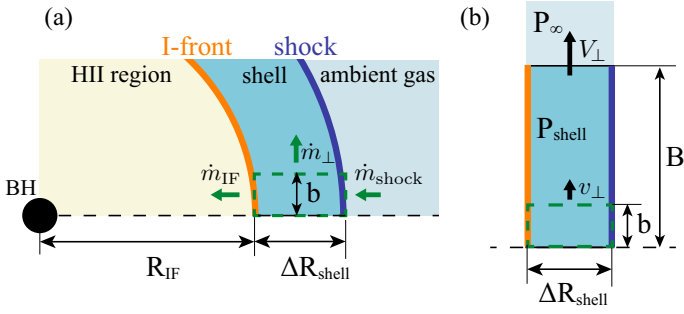


**Figure 2.** (a) The mass conservation in the cylindrical region of the shell illustrated by the dashed lines. (b) Approximation of the shell with vertical motion with a homogeneously expanding thin disk.

Here, we have assumed  $T_{\text{II}} = 4 \times 10^4$  K and  $\langle h\nu \rangle \approx 41$  eV for the power-law radiation spectrum  $L_\nu \propto \nu^{-1.5}$  with a lower cut-off at 13.6 eV. Therefore, for velocities higher than the critical velocity in Eq. (15),  $R_{\text{IF}} \approx r_{\text{neutral-flow}}$ , while for velocities lower than the critical value from Eqs. (8) and (11)–(13) we find:

$$R_{\text{IF}} \approx r_{\text{Strm}} = \left( \frac{12\pi\eta_0 c^4 m_{\text{p}}^2 G M_{\text{BH}}}{\langle h\nu \rangle \alpha_{\text{B}} L_{\text{Edd}}} \right)^{\frac{1}{3}} r_{\text{BHL,II}} \approx 120 r_{\text{BHL,II}}, \quad (16)$$

with the BHL radius for the ionized gas defined as

$$r_{\text{BHL,II}} = \frac{G M_{\text{BH}}}{v_{\text{II}}^2 + c_{\text{II}}^2} \quad (17)$$

$$\approx \begin{cases} \frac{G M_{\text{BH}}}{2c_{\text{II}}^2} \approx (110 \text{ au}) \left( \frac{M_{\text{BH}}}{100 M_{\odot}} \right) \left( \frac{c_{\text{II}}}{20 \text{ km/s}} \right)^{-2} & c_{\text{I}} < v_{\infty} < v_{\text{R}} \\ \frac{G M_{\text{BH}}}{v_{\infty}^2} \approx (100 \text{ au}) \left( \frac{M_{\text{BH}}}{100 M_{\odot}} \right) \left( \frac{v_{\infty}}{30 \text{ km/s}} \right)^{-2} & v_{\infty} \gg v_{\text{R}} \end{cases}.$$

The ratio of  $R_{\text{IF}}$  to  $r_{\text{BHL,II}}$  is independent of either  $M_{\text{BH}}$ ,  $n_{\infty}$ , or  $v_{\infty}$ , except for the dependence through  $T_{\text{II}}$ . Eq. (16) implies that the BHL radius is always much smaller than the size of the I-front in the RIAF regime.

## 2.2 Model of the shell

In the following, we extend the Park & Ricotti model to understand the property of the shells forming in the D-type flows. Specifically, we model the thickness of the shell  $\Delta R_{\text{shell}}$ , which is a critical parameter for the stability of the I-front, as we will see in Sec. 4. To model  $\Delta R_{\text{shell}}$ , we start from mass conservation in a cylindrical region of the shell with radius  $b$  from the axis of the BH motion (see Fig. 2 a). Below, we first estimate the mass flux at each surface of the cylinder and then derive the expression for the shell thickness. In this section, rather than restricting the model to isothermal shocks, we allow the sound speed in the shell,  $c_{\text{shell}}$ , to differ from that of the incident flow  $c_{\text{I}}$ . However, for simplicity, we assume that the temperature of the shell is kept constant at  $\approx 10^4$  K due to the strong temperature dependence of Ly $\alpha$  cooling (see also Appendix A2), with inefficient cooling below  $10^4$  K expected in a low-metallicity gas. We also neglect molecular hydrogen formation and cooling in the shell.

Let us start with obtaining the incoming mass flux

across the shock

$$\dot{m}_{\text{shock}} = \rho_{\infty} v_{\infty} \quad (18)$$

and outgoing mass flux across the I-front  $\dot{m}_{\text{IF}} = \rho_{\text{II}} v_{\text{II}}$ . Using Eqs. (6) and (7), we rewrite the mass flux in the HII region as

$$\dot{m}_{\text{IF}} = \frac{\rho_{\infty} (v_{\infty}^2 + c_{\text{I}}^2)}{2c_{\text{II}}}. \quad (19)$$

Note that the expression for  $\rho_{\text{II}}$  (Eq. 7), which is derived from total pressure equilibrium and conservation of mass flux, is valid even if the temperature changes across the shock.

Next, we estimate the outgoing mass flux at the lateral surface of the cylinder. Here, we make a rough approximation and regard the bow-like shell as a thin disk with radius  $B \sim O(R_{\text{IF}})$ , neglecting the curvature of the shell and the structure along the axis (Fig. 2b). The thermal pressure of the shocked gas,  $P_{\text{shell}}$ , which is higher than that of the ambient gas,  $P_{\infty}$ , causes the radial expansion of the disk. We estimate the gas velocity at the outer edge as  $V_{\perp} \sim O(v_{\infty})$ , considering the approximate balance between the thermal pressure of the shell  $P_{\text{shell}} \approx \rho_{\infty} v_{\infty}^2$  and the ram pressure of the ambient gas  $\rho_{\infty} V_{\perp}^2$  in the rest frame of the edge. Since the vertical velocity  $v_{\perp}$  is proportional to  $b$  in a uniformly expanding disk, we model it as

$$v_{\perp} = \frac{b}{B} V_{\perp} \equiv \alpha \frac{b}{R_{\text{IF}}} v_{\infty}, \quad (20)$$

where we introduce an  $O(1)$  numerical factor  $\alpha$  in the last expression to absorb the uncertainties of the model. The density of the shell is determined by the approximate balance between the inner thermal pressure and outer ram pressure at the shock as

$$\rho_{\text{shell}} \approx \left( \frac{v_{\infty}}{c_{\text{shell}}} \right)^2 \rho_{\infty}. \quad (21)$$

Therefore, from Eqs. (20) and (21), the vertical mass flux  $\dot{m}_{\perp} = \rho_{\text{shell}} v_{\perp}$  at radius  $b$  is given by

$$\dot{m}_{\perp} = \alpha \left( \frac{b}{R_{\text{IF}}} \right) \left( \frac{v_{\infty}}{c_{\text{shell}}} \right)^2 \rho_{\infty} v_{\infty}. \quad (22)$$

Finally, we obtain  $\Delta R_{\text{shell}}$  considering mass conservation. The equation for the conservation of mass inside the cylinder with radius  $b$  and length  $\Delta R_{\text{shell}}$  is given by

$$\dot{m}_{\text{shock}} \pi b^2 - \dot{m}_{\text{IF}} \pi b^2 - \dot{m}_{\perp} 2\pi b \Delta R_{\text{shell}} = 0, \quad (23)$$

where the first, second, and third terms correspond to the flows through the shock, I-front, and lateral surface of the cylinder, respectively. With Eqs. (19), (18) and (22), Eq. (23) can be solved for  $\Delta R_{\text{shell}}$  as

$$\Delta R_{\text{shell}} = \frac{1}{2\alpha} \left( \frac{v_{\infty}}{c_{\text{shell}}} \right)^{-2} \left( 1 - \frac{v_{\infty}^2 + c_{\text{I}}^2}{2c_{\text{II}} v_{\infty}} \right) R_{\text{IF}} \quad (24)$$

$$\approx \frac{1}{2\alpha} \left( \frac{v_{\infty}}{c_{\text{shell}}} \right)^{-2} \left( 1 - \frac{v_{\infty}}{v_{\text{R}}} \right) R_{\text{IF}}, \quad (25)$$

where we have made an approximation  $c_{\text{I}} \ll v_{\infty}$  and used the approximate expression of the critical velocity  $v_{\text{R}} \approx 2c_{\text{II}}$  (Eq. 3) in the last equation. Later, we will determine the  $O(1)$  value for  $\alpha$  and the effective temperature of ionized region  $T_{\text{II}}$  by comparing Eq. (24) to the simulation results. Here we

define  $T_{\text{II}}$  as an effective temperature because it absorbs the uncertainties coming from the temperature variation inside the HII region and the simplifying assumptions in modelling  $\dot{m}_{\text{IF}}$ . This expression implies that  $\Delta R_{\text{shell}}$  approaches zero as  $v_{\infty}$  approaches  $v_{\text{R}}$  from the lower side. Thus, we can consider that the transition from the D- to R-type flow occurs at  $v_{\text{R}}$ , not only because the R-type I-fronts are allowed only for  $v_{\infty} > v_{\text{R}}$ , but also because the shells in the D-type flows can have finite thickness only for  $v_{\infty} < v_{\text{R}}$ .

Before closing this section, we shortly discuss the column density of the shell. From Eqs. (21) and (25), we can roughly estimate it as  $m_{\text{p}} \Delta N_{\text{shell}} = \rho_{\text{shell}} \Delta R_{\text{shell}} \sim \rho_{\infty} R_{\text{IF}} (1 - v_{\infty}/v_{\text{R}})$ , omitting the  $O(1)$  numerical factors. Using Eqs. (16) and (17), for velocities  $v_{\infty} < v_{\text{R}}$ , we obtain the shell column density:

$$\Delta N_{\text{shell}} \approx (3.0 \times 10^{21} \text{ cm}^{-2}) \left(1 - \frac{v_{\infty}}{v_{\text{R}}}\right) \left(\frac{n_{\infty} M_{\text{BH}}}{10^6 M_{\odot} \text{ cm}^{-3}}\right), \quad (26)$$

which is proportional to  $n_{\infty} M_{\text{BH}}$  with the dependence on  $v_{\infty}$  through the factor  $(1 - v_{\infty}/v_{\text{R}})$ . We see that the shell is typically optically thick to ionizing radiation for  $n_{\infty} M_{\text{BH}} > 10^3 M_{\odot} \text{ cm}^{-3}$ .

### 3 3D RADIATION HYDRODYNAMICS SIMULATIONS

We perform 3D radiation hydrodynamics simulations, using the same code as in Sugimura et al. (2017, 2018), which is a modified version of a public grid-based multidimensional magnetohydrodynamics code PLUTO 4.1 (Mignone et al. 2007). In the code, a module for 1D multi-frequency radiation transfer coupled with primordial chemical network and thermodynamics is implemented (Kuiper et al. 2010a,b, 2011; Kuiper & Klessen 2013; Hosokawa et al. 2016). As mentioned in the introduction, 3D simulations are necessary to study the instability of I-fronts, but they are computationally expensive and difficult to interpret because of the complicated interplay of various physical processes. Therefore, we perform 3D simulations of gas dynamics on the scale of I-front, assuming constant luminosity and neglecting BH gravity, to study the structure and instability of I-front in a well-controlled numerical experiment.

We adopt a spherical computational region with the BH at the origin  $r = 0$  and assume that gas flows into the computational region from the positive  $x$ -direction ( $\theta = \pi/2$  and  $\phi = 0$ ). We use logarithmically spaced grids in the  $r$ -direction for  $0.1 R_{\text{IF}} < r < 10 R_{\text{IF}}$  and linearly spaced grids in the  $\theta$ - and  $\phi$ -directions for  $0 < \theta < \pi$  and  $0 < \phi < 2\pi$ , respectively. To determine the radial range, we obtain  $R_{\text{IF}}$  by performing test runs before the science runs.

We use nested grids in each direction, to achieve sufficiently high resolution around the part of the I-front near the axis of the BH motion, where the instability is likely to start growing. In the  $r$ -direction, we set the base level grids with  $N_r = 64$ , replace the half of the grids around  $r = R_{\text{IF}}$  with two times finer next level grids, and repeat a similar refinement process for the highest level grids. Similarly, in the  $\theta$ - and  $\phi$ -directions, we set the base level grids with  $N_{\theta} = 80$  and  $N_{\phi} = 80$ , and repeatedly replace the highest level grids around  $\theta = \pi/2$  and  $\phi = 0$  with finer grids. In the typical runs, we repeat the refinement process three times for the

$r$ - and  $\phi$ -directions and two times for the  $\theta$ -direction, resulting in approximately cubic ( $\Delta r \approx r \Delta \theta \approx r \sin \theta \Delta \phi$ ) minimum cells with side length  $\Delta x \approx 0.01 R_{\text{IF}}$ . The effective resolution of these cells is  $N_r \times N_{\theta} \times N_{\phi} = 512 \times 320 \times 640$ . For the case of D-type flow with a thin shell, we refine the grids one more time in each direction requiring that the shell thickness is resolved by at least 5 cells, to avoid obtaining artificially stable results due to the lack of the resolution.

We apply flow-in outer boundary condition on the up-wind side of the hemisphere ( $0 < \phi < \pi/2$  and  $3\pi/2 < \phi < 2\pi$ ) with the boundary values set to those of the ambient gas, and flow-out boundary condition on the down-wind side. For the inner boundary, we introduce a virtual sink cell where the physical quantities are determined by the advection through the boundary with the conservation laws. To alleviate having a short time step due to polar cells with small azimuthal length  $r \sin \theta \Delta \phi$ , we limit the hydrodynamic calculations to the range of  $0.2 < \theta < \pi - 0.2$  and instead introduce virtual cells with radial extents set by the radial grids in the polar regions. We neglect the BH gravity in our simulations because the BHL radius is 10 times smaller than the inner boundary at  $0.1 R_{\text{IF}}$  (see Eq. 16), hence thermal and ram pressure dominate the dynamics of gas in our computational domain. In the liner growth regime, BH gravity should not affect the development of the instability at the I-front because, not only the BH gravity is weak, but also the gravitational field is smooth on the scale of the I-front. However, the non-linear evolution of the instability may be altered by the BH gravity because clumps formed as a result of the front fragmentation may gravitationally focused toward the BH. We plan to study this process with 3D simulations including BH gravity and radiation coupled to the accretion rate in future works. We also neglect gas self-gravity in this work. Approximating the size of fragmented clumps with the shell thickness  $\Delta R_{\text{shell}} \sim 10^3 \text{ au} ((\Delta R_{\text{shell}}/R_{\text{IF}})/0.1)(M_{\text{BH}}/10^2 M_{\odot})$  (Eqs. 16 and 17 with  $c_{\text{II}} = 20 \text{ km/s}$ ) and comparing it with the Jeans length  $\lambda_{\text{J}} \equiv \sqrt{\pi} c_{\text{s}}/\sqrt{\rho} \sim 3 \times 10^5 \text{ au} (T_{\text{I}}/10^4 \text{ K})^{1/2} (n_{\text{shell}}/10^6 \text{ cm}^{-3})^{-1/2}$ , we estimate that the self-gravity is negligible for BH masses  $M_{\text{BH}} \lesssim 3 \times 10^4 M_{\odot} (T_{\text{I}}/10^4 \text{ K})^{1/2} (n_{\text{shell}}/10^6 \text{ cm}^{-3})^{-1/2}$ , but the shell and its fragment may be self-gravitating for higher BH mass.

For the initial conditions, we assume uniform density and velocity with the ambient values and add 10 percent random density perturbations to seed the instability. The results, after saturation of the instability, are insensitive to the amplitude of the initial perturbations, which we confirm by performing additional simulations with 10 times smaller perturbations. This also suggests that the choice of the power spectrum of initial perturbations does not affect our main conclusions: indeed the instability develops similarly (although less rapidly) even without adding perturbations to the initial conditions. However, a large-scale gradient of the background density field may cause some effects. A density gradient in the direction parallel to the BH motion modulates the incident flow density at the I-front, leading to a back and forth motion of the I-front, and hence a modulation of the relative velocity of the flow with respect to the I-front. We expect that such case can be understood by combining the results for different velocity cases. A density gradient in the direction perpendicular to the BH motion produces a net angular momentum to the gas near the BH,

due to the asymmetry of angular momentum carried by accreted gas. Sugimura et al. (2018), who studied the effect of gas angular momentum on accretion of non-moving BHs, found that the accretion rate is strongly suppressed if the accretion disk formed as a result of gas angular momentum is comparable to the Bondi radius. The effect of gas angular momentum in the case of moving BH in a medium with a density gradient is yet to be studied, but it will be the topic of future work.

Below, we describe the parameters examined in our simulations. In the reference runs, we set the parameters as follows: the ambient density  $n_\infty = 10^5 \text{ cm}^{-3}$ ; the BH mass  $M_{\text{BH}} = 10^2 M_\odot$ , which is used to calculate the luminosity; the ambient temperature  $T_\infty = 10^4 \text{ K}$ , with a lower temperature floor at  $T_\infty$  imposed for simplicity; and the BH velocities  $v_\infty/c_\infty = 2, 4$  and  $7$ , where  $c_\infty$  is sound speed in the neutral gas with temperature  $T_\infty$ . We set the constant luminosity to  $L = 2 \times 10^{39} \text{ erg s}^{-1}$ , the value predicted by the Park & Ricotti model for  $v_\infty/c_\infty = 4$  with Eqs. (9), (11), and (12). We assume a power-law spectrum  $L_\nu \propto \nu^{-1.5}$  with a lower cut-off at  $13.6 \text{ eV}$  (e.g., Park & Ricotti 2011). As we will see in the next section, the above three velocities correspond to the three different regions of flow structures shown in Fig. 1: the stable D-type flow (Region I), the unstable D-type flow (Region II), and the R-type flow (Region III), respectively. In addition to the reference runs, we perform the runs with various BH velocities in the range of  $1.5 \leq v_\infty/c_\infty \leq 10$  to study the velocity dependence in detail. To investigate the dependence on the density and BH mass, we also perform runs with  $n_\infty = 10^4 \text{ cm}^{-3}$  and luminosity for a  $M_{\text{BH}} = 10^2 M_\odot$  BH ( $L = 2 \times 10^{37} \text{ erg s}^{-1}$ ), and density  $n_\infty = 10^3 \text{ cm}^{-3}$  with luminosity for a  $M_{\text{BH}} = 10^2 M_\odot$  BH ( $L = 2 \times 10^{35} \text{ erg s}^{-1}$ ), and  $n_\infty = 10^4$  with luminosity for a  $M_{\text{BH}} = 10^3 M_\odot$  BH ( $L = 2 \times 10^{40} \text{ erg s}^{-1}$ ). Note that all the cases examined in this paper are in the RIAF regime where  $L \propto \dot{M}^2/M_{\text{BH}} \propto \dot{M}_{\text{BH}}^3 n_\infty^2$  (see Eqs. 8, 11, and 12).

## 4 RESULTS

### 4.1 Region I: stable D-type flows

Figure 3 shows the snapshot of the steady-state flow for the run with  $n_\infty = 10^5 \text{ cm}^{-3}$ ,  $M_{\text{BH}} = 10^2 M_\odot$ ,  $T_\infty = 10^4 \text{ K}$ , and  $v_\infty/c_\infty = 2$ . We perform this run as the reference case for the stable D-type flows in the Region I of Figure 1. As expected, we see that a stable, dense shell forms between the D-type I-front and the preceding shock, alike a bow shock around a blunt body (see, e.g., Yalinewich & Sari 2016; Keshet & Naor 2016, for recent studies).

Let us investigate the structure of the flow in detail. In the HII region, the gas is heated to the equilibrium temperature  $T_{\text{II}} \approx 4 - 5 \times 10^4 \text{ K}$ , determined by the balance of the photo-ionization heating and the Ly $\alpha$  and free-free cooling. The shock is isothermal due to the efficient Ly $\alpha$  cooling in the neutral gas, and the density jump in the shell is  $(v_\infty/c_\infty)^2 \approx 4$  of the ambient value. As considered in the analytical model in Sec. 2, the gas motion is approximately plane-parallel except for inside the shell, where the tangentially diverging motion has a significant effect on the streamlines. The shell is rather thick ( $\Delta R_{\text{shell}}/R_{\text{IF}} \sim 0.1$ ) and stable. The size of the I-front,  $R_{\text{IF}} \sim 2 \times 10^4 \text{ au}$ , agrees with the

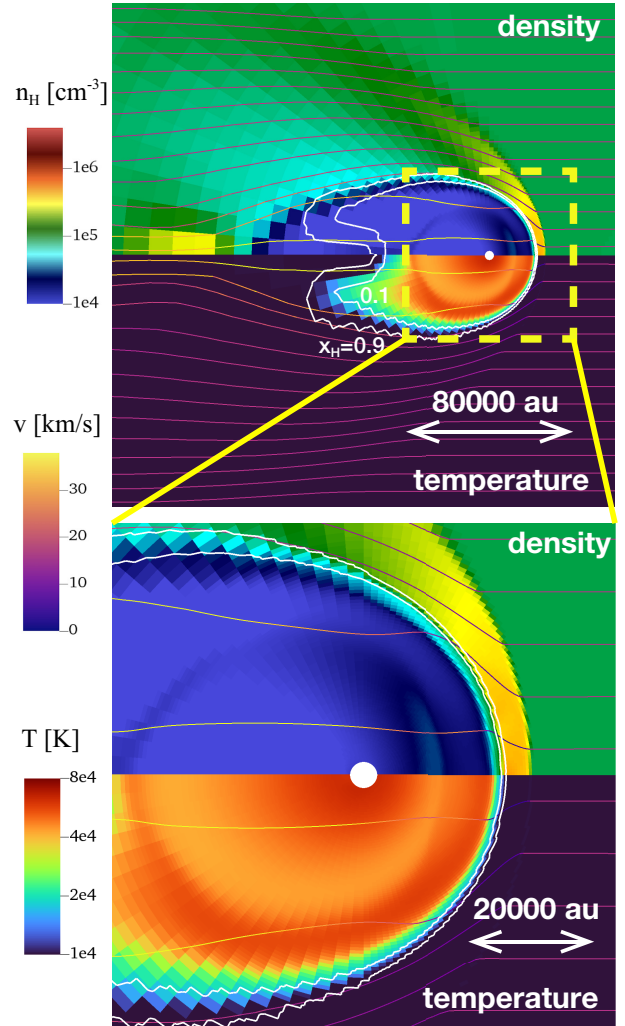


**Figure 3.** The snapshots of the steady-state flow in the run with  $n_\infty = 10^5 \text{ cm}^{-3}$ ,  $M_{\text{BH}} = 10^2 M_\odot$ ,  $T_\infty = 10^4 \text{ K}$ , and  $v_\infty/c_\infty = 2$ . The bottom panel is a zoom-in view of the top panel where the entire HII bubble is displayed. In each panel, we show the xy-slice of the density (upper) and the temperature (lower), together with the velocity streamlines. The outer and inner white contours correspond to the surfaces of the neutral fraction  $x_{\text{H}} = 0.9$  and  $0.1$ , respectively. The gas is moving from the right side to the left, with the BH located at the center of the sink region (white circle).

analytic Strömgen radius in Eq. (13). In general, the flow structure is consistent with previous 2D simulations in PR13 and agrees with the analytical model.

To understand the properties of the shell and its stability, we investigate the dependence of the shell thickness on the BH velocity, by performing runs with various BH velocities  $v_\infty/c_\infty = 1.5 - 3$  for  $n_\infty = 10^5 \text{ cm}^{-3}$  and  $M_{\text{BH}} = 10^2 M_\odot$ . We observe stable D-type flows for the velocity range mentioned above, but the shell becomes unstable or disappears (the I-front becomes R-type) for velocities  $v_\infty/c_\infty > 3$ , as we will see in the next section.

Figure 4 summarizes the main results found in this paper with regard to the stability of the I-front. The points in the figure show the ratio of the shell thickness to the size of the I-front,  $\Delta R_{\text{shell}}/R_{\text{IF}}$ , as a function of  $v_\infty/c_\infty$  for a large set of simulations, as shown in the legend. We see that the



ratio becomes smaller, *i.e.*, the shell becomes thinner, with increasing  $v_\infty/c_\infty$ . The filled symbols refer to simulations in which the shell is stable, while open symbols refer to simulations with unstable shells.

The solid lines in the figure show  $\Delta R_{\text{shell}}/R_{\text{IF}}$  from the analytical model described by Eq. (24) in Sec. 2.2, for several values of  $T_{\text{II}}$ , together with the arrows indicating the values of  $v_{\text{R}}$ , at which the thickness becomes zero according to the model. For the moment, we focus on the curve for  $T_{\text{II}} = 6 \times 10^4$  K because the temperature inside the HII region has approximately this value in the runs with  $n_\infty = 10^5 \text{ cm}^{-3}$  and  $M_{\text{BH}} = 10^2 M_\odot$  (see Figure 3). With the numerical factor set to  $\alpha = 0.5$ , the analytical curve for  $T_{\text{II}} = 4 \times 10^4$  K shows good agreement with the simulation results for  $n_\infty = 10^5 \text{ cm}^{-3}$  and  $M_{\text{BH}} = 10^2 M_\odot$ . The agreement is good also for all the other simulations in the figure, justifying the validity of our analytical model, as well as the choice of  $\alpha = 0.5$ . The analytical model predicts that the thickness approaches zero as  $v_\infty$  approaches  $v_{\text{R}}$ . In the runs with  $n_\infty = 10^5 \text{ cm}^{-3}$  and  $M_{\text{BH}} = 10^2 M_\odot$ , however, the shell becomes unstable before the velocity reaches  $v_{\text{R}}$ , as indicated by the open symbols.

We also investigate the dependence of shell thickness on  $n_\infty$  and  $M_{\text{BH}}$ , in addition to the dependence on  $v_\infty$ . We performed runs with various  $v_\infty$ , assuming  $(n_\infty, M_{\text{BH}}) = (10^4 \text{ cm}^{-3}, 10^2 M_\odot)$ ,  $(10^3 \text{ cm}^{-3}, 10^2 M_\odot)$ , and  $(10^3 \text{ cm}^{-3}, 10^3 M_\odot)$ , and plot  $\Delta R_{\text{shell}}/R_{\text{IF}}$  of the stable D-type flows in Figure 4. We see that  $\Delta R_{\text{shell}}/R_{\text{IF}}$  becomes smaller when decreasing  $n_\infty$  or  $M_{\text{BH}}$ . It appears that  $\Delta R_{\text{shell}}/R_{\text{IF}}$  is proportional to the parameter combination  $M_{\text{BH}} n_\infty$ .

According to our model, the shell thickness depends on parameters other than  $v_\infty$  only because of changes of the sound speed inside the HII region,  $c_{\text{II}}$ . We will show below that  $c_{\text{II}}$  depends on  $M_{\text{BH}} n_\infty$ , and that this dependence can be attributed to changes in the temperature profile inside the ionized region. In Fig. 5, we plot the upstream temperature profiles along the axis of BH motion in the runs with  $v_\infty/c_\infty = 2$  and different  $n_\infty$  and  $M_{\text{BH}}$ . We normalize the radius by the size of the I-front to directly compare the temperature profiles. We see in Fig. 5 that the steepness of the temperature rise inside the HII region has significant differences among the runs. For the run with BH mass  $M_{\text{BH}} = 10^2 M_\odot$  and  $n_\infty = 10^5 \text{ cm}^{-3}$ , the temperature rapidly reaches the almost constant value  $5-6 \times 10^4$  K inside the HII region, while the rise in temperature becomes slower as  $n_\infty$  decreases. Therefore, in the lower-density case with  $n_\infty \leq 10^4 \text{ cm}^{-3}$ , we need to define an effective temperature inside the HII region to be used in the analytical model. We set the effective temperature to  $T_{\text{II}} = 1.8 \times 10^4$  K and  $3 \times 10^4$  K for the case with  $n_\infty = 10^3$  and  $10^4 \text{ cm}^{-3}$ , respectively. These are values measured near the ionization front. In addition, with these values adopted, the analytical curves for  $\Delta R_{\text{shell}}/R_{\text{IF}}$  are in good agreement with the numerical results shown in Fig. 4. For the case with  $n_\infty = 10^3$ , we also perform runs with temperature upstream of the ionization front  $T_\infty = T_{\text{I}} = 30$  K, hence assuming that X-ray preheating is negligible (see Appendix. A2 about X-ray preheating). In these runs, we observe that the temperature rapidly increases from  $T_{\text{I}} = 30$  K to  $T_{\text{shell}} = 10^4$  K at the shock. The thickness of the bow-shock is slightly larger than in the corresponding runs with  $T_\infty = 10^4$  K and is well reproduced by the analytical model with  $T_{\text{I}} = 30$  K and  $T_{\text{shell}} = 10^4$  K, be-

cause the  $(1 - (v_\infty^2 + c_{\text{I}}^2)/2c_{\text{II}}v_\infty)$  term in Eq. (24) is larger when  $c_{\text{I}}$  is lower. As for the  $M_{\text{BH}}$  dependence, the run with  $(n_\infty, M_{\text{BH}}) = (10^4 \text{ cm}^{-3}, 10^3 M_\odot)$  has almost the same temperature profile as the run with  $(n_\infty, M_{\text{BH}}) = (10^5 \text{ cm}^{-3}, 10^2 M_\odot)$ .

Next, let us explain how the temperature profile depends on  $n_\infty$  and  $M_{\text{BH}}$ . The temperature just inside the I-front is roughly determined by the balance between the photo-ionization heating and the Ly $\alpha$  cooling. The gas inside the I-front is almost fully ionized, *i.e.*,  $x_{\text{HI}} \ll 1$  and  $x_{\text{HII}} = x_e \approx 1$ , where  $x_{\text{HI}}$ ,  $x_{\text{HII}}$ , and  $x_e$  are the hydrogen neutral fraction, ionized fraction, and the electron fraction, respectively. The gas is roughly in photo-ionization equilibrium:  $k_{\text{ion}} n_{\text{H}} x_{\text{HI}} = \alpha_{\text{B}} n_{\text{H}}^2 x_{\text{HII}} x_e \approx \alpha_{\text{B}} n_{\text{H}}^2$ , where  $k_{\text{ion}}$  is the hydrogen photo-ionization rate. Thus, the photo-ionization heating rate per unit volume is  $\Gamma = \Delta E k_{\text{ion}} n_{\text{H}} x_{\text{HI}} \approx \Delta E \alpha_{\text{B}} n_{\text{H}}^2$ , where  $\Delta E = \langle h\nu \rangle_{\text{ion}} - 13.6 \text{ eV}$  is the mean energy deposited into the gas per photo-ionization. The Ly $\alpha$  cooling rate can be written as  $\Lambda = \tilde{\Lambda}_{\text{Ly}\alpha} n_{\text{H}}^2 x_e x_{\text{HI}} \approx \tilde{\Lambda}_{\text{Ly}\alpha} n_{\text{H}}^2 x_{\text{HI}}$  with a  $T$ -dependent coefficient  $\tilde{\Lambda}_{\text{Ly}\alpha}$ . As  $\alpha_{\text{B}}$  and  $\tilde{\Lambda}_{\text{Ly}\alpha}$  are decreasing and increasing functions of  $T$ , respectively, the equilibrium temperature (*i.e.*,  $\Gamma = \Lambda$ ) is higher if the neutral fraction behind the I-front,  $x_{\text{HI}}$ , is lower.

In ionization equilibrium,  $x_{\text{HI}}$  is inversely proportional to the ionization parameter,  $\xi \equiv F_{\text{ion}}/n_{\text{II}}$ , where  $F_{\text{ion}}$  is the flux of ionizing radiation. Since the absorption of the ionizing photons inside the HII region is insignificant except for the extreme vicinity of the I-front, we assume optically thin flux in our estimate. Then, approximating the size of I-front with the Strömberg radius  $r_{\text{Strm}}$  (Eq. 13), we obtain  $\xi$  slightly inside the I-front as

$$\xi = \frac{L}{4\pi r_{\text{Strm}}^2 n_{\text{II}}} \propto L^{1/3} n_{\text{II}}^{1/3}, \quad (27)$$

where we ignore the  $T_{\text{II}}$  dependence in the last expression. From Eqs. (8), and (11)-(12), the analytical model predicts that  $L$  is proportional to  $M_{\text{BH}}^3 n_\infty^2$  in the RIAF regime. Therefore, from Eq. (27), the dependence of  $\xi$  on  $M_{\text{BH}}$  and  $n_\infty$  is

$$x_{\text{HI}}^{-1} \propto \xi \propto M_{\text{BH}} n_\infty. \quad (28)$$

This explains why the temperature rise inside the HII region is steeper in the runs with larger  $n_\infty$  for fixed  $M_{\text{BH}}$ , as well as why we obtain the same temperature profiles in runs having the same  $n_\infty M_{\text{BH}}$ .

## 4.2 Region II: unstable D-type flows

As we increase  $v_\infty$ , the dense shell in the D-type flow becomes unstable. As a reference case for the unstable D-type flow in the Region II of Fig. 1, we perform the run with  $n_\infty = 10^5 \text{ cm}^{-3}$ ,  $M_{\text{BH}} = 10^2 M_\odot$ ,  $T_\infty = 10^4$  K, and  $v_\infty/c_\infty = 4$ . We show a snapshot of the flow structure after the instability is fully developed and saturated in Fig. 6. We also provide a corresponding 3D view in Fig. 7. The shell is destroyed by the eruptive expansions of the I-front launched from various places, with dense clumps forming in the gaps of the I-front.

The instability in this range of  $v_\infty$  was seen in the previous 2D simulations of PR13. However, the way the instability grows is significantly different in 2D versus 3D simulations (see Fig.8 of PR13), as we have also confirmed by performing 2D comparative runs. Although the structures due to the instability are seen in various directions in 3D, they tend to converge to the axis of BH motion in 2D due

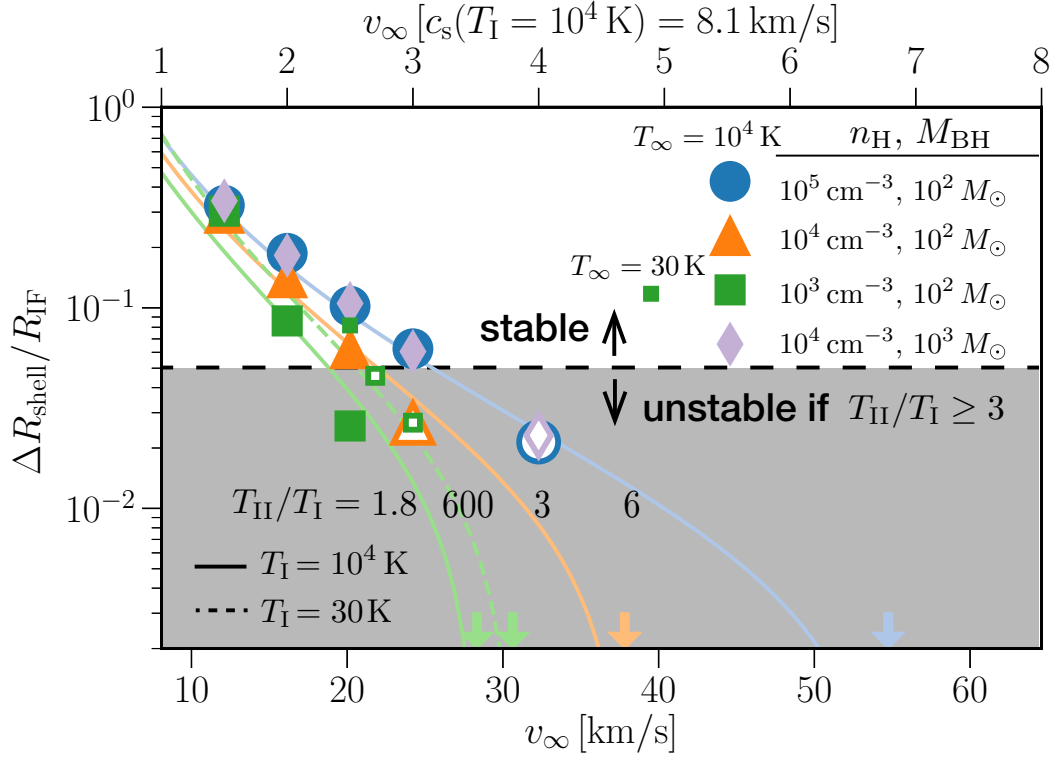


**Figure 4.** The ratio of the shell thickness to the size of ionization front,  $\Delta R_{\text{shell}}/R_{\text{IF}}$ , as a function of  $v_{\infty}$ . The symbols show the results from the simulations:  $(n_{\infty}, M_{\text{BH}}) = (10^5 \text{ cm}^{-3}, 10^2 M_{\odot})$  (blue circles),  $(10^4 \text{ cm}^{-3}, 10^2 M_{\odot})$  (orange triangles),  $(10^3 \text{ cm}^{-3}, 10^2 M_{\odot})$  (green squares), and  $(10^4 \text{ cm}^{-3}, 10^3 M_{\odot})$  (purple diamonds). The large symbols are for the runs with  $T_{\infty} = 10^4 \text{ K}$  and the small ones are for simulations with  $T_{\infty} = 30 \text{ K}$ . The solid lines show the analytical model in Eq. (24) setting  $\alpha = 0.5$ ,  $T_{\text{I}} = 10^4 \text{ K}$  and  $T_{\text{II}} = 1.8 \times 10^4$  (green line),  $3 \times 10^4$  (orange line), and  $6 \times 10^4$  (blue line). The green dashed line refers to a model with  $T_{\text{I}} = 30 \text{ K}$  and  $T_{\text{shell}} = 10^4 \text{ K}$ . The lines are also labelled by the temperature jump  $\Delta T \equiv T_{\text{II}}/T_{\text{I}}$  across the I-front, that is an important parameter in predicting the stability of the front. The arrows indicate the value of  $v_{\text{R}}$  given by Eq. (3), at which the analytical model predicts that the thickness of the shell becomes zero. The filled and open symbols correspond to the stable and unstable shells, respectively. As discussed in the text, the front is unstable only if  $\Delta R_{\text{shell}}/R_{\text{IF}} < 0.05$  and  $\Delta T \geq 3$ , as demarcated by the black dashed line.

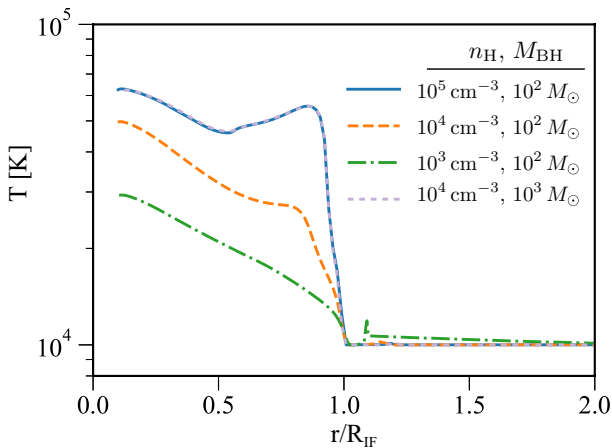


**Figure 5.** Upstream temperature profiles along the axis of BH motion in the runs with  $v_{\infty}/c_{\infty} = 2$  and different  $n_{\infty}$  and  $M_{\text{BH}}$ . The colors represent  $n_{\infty}$  and  $M_{\text{BH}}$  in the same way as Fig. 4. The radius is normalized by the size of I-front,  $R_{\text{IF}}/10^4 \text{ au} = 2.2, 1.3, 0.92$  and  $2.4$  for the runs with  $(n_{\infty}, M_{\text{BH}}) = (10^5 \text{ cm}^{-3}, 10^2 M_{\odot})$ ,  $(10^4 \text{ cm}^{-3}, 10^2 M_{\odot})$ ,  $(10^3 \text{ cm}^{-3}, 10^2 M_{\odot})$ , and  $(10^4 \text{ cm}^{-3}, 10^3 M_{\odot})$ , respectively. The profiles for  $(n_{\infty}, M_{\text{BH}}) = (10^5 \text{ cm}^{-3}, 10^2 M_{\odot})$  and  $(10^4 \text{ cm}^{-3}, 10^3 M_{\odot})$  almost completely overlap with each other.

to the assumed axisymmetry, making the structures more ordered and stronger in 2D than in 3D. Furthermore, we observe that the instability can be artificially seeded near the axis in 2D due to the singularity of the spherical coordinates.

The instability can be understood as the instability of a thin shell between the D-type I-front and the shock, studied in previous literature. This instability was found analytically using linear analysis by Giuliani (1979) and confirmed in 2D (Garcia-Segura & Franco 1996) and 3D (Whalen & Norman 2008a,b) simulations of an expanding D-type I-fronts around massive stars. As mentioned in Garcia-Segura & Franco (1996), this instability is caused by a mechanism similar to that of the thin-shell instability of an expanding hot bubble in a cold ambient gas found by Vishniac (1983). In both cases, the thermal pressure of inner hot gas and the ram pressure of external cold gas balanced each other in the unperturbed state, but a force imbalance is introduced in the presence of shell distortions because the force from the thermal pressure is orthogonal to the surface but the ram-pressure force is parallel to the flow, enhancing the front distortion. Using linear perturbation analysis, under the assumption of plane-parallel and infinitely-thin shell, Giuliani (1979) showed that the modes with wavelength  $\lambda$  several



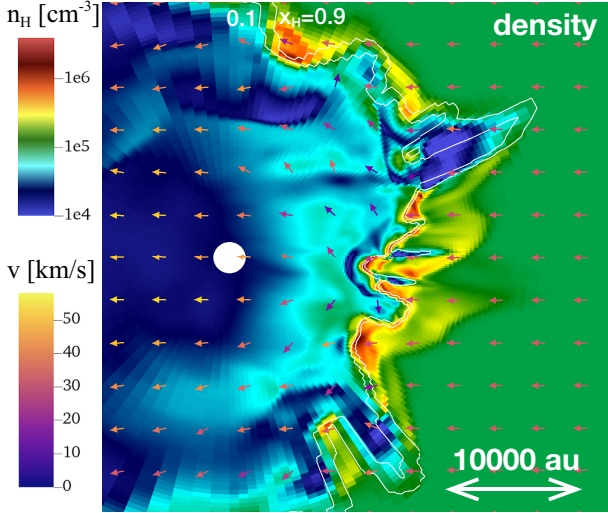


**Figure 6.** The same as Fig. 3 but for the run with  $n_\infty = 10^5 \text{ cm}^{-3}$ ,  $M_{\text{BH}} = 10^2 M_\odot$ ,  $T_\infty = 10^4 \text{ K}$ , and  $v_\infty/c_\infty = 4$  at a time after the instability is fully developed and saturated.

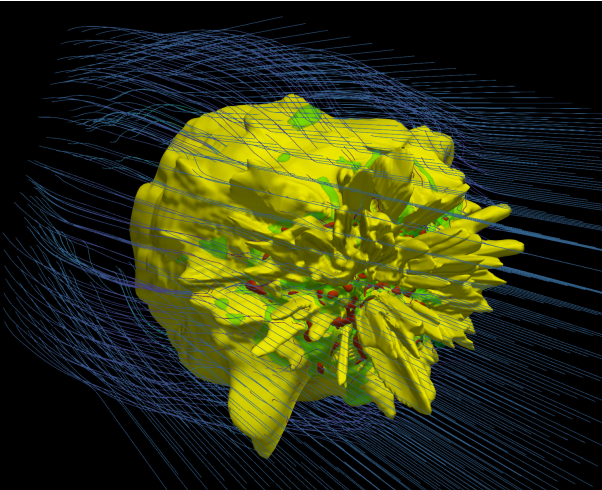


**Figure 7.** A 3D view of the flow structure corresponding to the 2D slice snapshot in Fig. 6. We illustrate the I-front (yellow), together with the density (green and red) and velocity (streamlines) fields. The green and red contours correspond to  $n_{\text{H}} = 5 \times 10^5$  and  $10^6 \text{ cm}^{-3}$ , respectively.

times greater than the recombination length,  $d_r \equiv c_{\text{II}}/n_{\text{II}}\alpha_{\text{B}}$ , are unstable.

This result implies that the shell around a moving BH is unstable if the following two conditions are satisfied. Firstly, the perturbed front displacement  $\delta r$  needs to be larger than the shell thickness in order for the mode to grow. Since in the linear regime the front displacement is  $\delta r \sim A\lambda$  with  $A \ll 1$ , we get  $\lambda > \Delta R_{\text{shell}}/A$ . Since the longest wavelengths growing modes have  $\lambda < R_{\text{IF}}$ , we find that unstable modes exist only in the range  $\Delta R_{\text{shell}}/A < \lambda < R_{\text{IF}}$ . Therefore,  $\Delta R_{\text{IF}}/A \leq R_{\text{IF}}$ , that is  $\Delta R_{\text{IF}}/R_{\text{IF}} \leq A$ , is a necessary condition for the instability. Secondly, the condition  $d_r \ll R_{\text{IF}}$  is required, in order for some of the above modes to be unstable. In the case examined in this paper, the second condition is safely

satisfied because  $d_r \sim 20 \text{ au} (n_{\text{II}}/10^5 \text{ cm}^{-3})^{-1} (T_{\text{II}}/4 \times 10^4 \text{ K})^{3/2}$  is generally much smaller than  $R_{\text{IF}}$ .

To understand the condition for the instability using the simulations, we focus on the relationship between the instability and the shell thickness. In Fig. 4 we plot  $\Delta R_{\text{shell}}/R_{\text{IF}}$  for the unstable simulations (open symbols), along with the results for the stable simulations (solid symbols) discussed in Sec. 4.1. Since the shell thickness is not a well-defined quantity for the unstable simulations, we plot  $\Delta R_{\text{shell}}/R_{\text{IF}}$  obtained from lower-resolution runs where the instability was suppressed due to lack of resolution. These values should be viewed with caution because the shell thickness is resolved only with one or two cells. In Fig. 4, except for the case with  $(n_\infty, M_{\text{BH}}, T_\infty) = (10^3 \text{ cm}^{-3}, 10^2 M_\odot, 10^4 \text{ K})$ , we see that the shells are unstable if

$$\Delta R_{\text{shell}}/R_{\text{IF}} < 0.05, \quad (29)$$

as demarcated by the dashed line. Using Eq. (25), we can rewrite the condition  $\Delta R_{\text{shell}}/R_{\text{IF}} = 0.05$  into the form  $(v_\infty/c_1)^{-2} (1 - (v_\infty/c_1)(c_1/v_{\text{R}})) = 0.05$ , which is a quadratic equation of  $v_\infty$  for fixed  $c_1 = 8.1 \text{ km/s} (T_{\text{I}}/10^4 \text{ K})^{1/2}$  and  $v_{\text{R}} \approx 2c_{\text{II}} = 46 \text{ km/s} (T_{\text{II}}/4 \times 10^4 \text{ K})^{1/2}$ . The positive solution of the above equation is

$$v_{\text{crit}} = \frac{5}{\sqrt{2\Delta_{\mathcal{T}}}} \left( \sqrt{1 + 1.6\Delta_{\mathcal{T}}} - 1 \right) c_\infty, \quad (30)$$

where we have assumed  $c_1 = c_\infty$  and  $\Delta_{\mathcal{T}} \equiv T_{\text{II}}/T_{\text{I}}$ . Therefore the D-type I-front is unstable in the velocity range  $v_{\text{crit}} < v_\infty < v_{\text{R}}$ . As also evident in Fig. 4, the velocity range in which the shell is unstable is rather large for large temperature jump  $\Delta_{\mathcal{T}}$  across the I-front, but tends to become very narrow and nearly disappear when  $\Delta_{\mathcal{T}} \rightarrow 1$ . As expected, in the run shown in Fig. 6, we observe the formation of an extremely thin shell before the instability grows and destroys the shell, supporting the hypothesis that the instability seen in this run is the thin-shell instability found by Giuliani (1979).

The instability criteria above, however, is a necessary but not a sufficient condition, as exemplified by the run with  $n_\infty = 10^3 \text{ cm}^{-3}$ ,  $M_{\text{BH}} = 10^2 M_\odot$ ,  $T_\infty = 10^4 \text{ K}$ , and  $v_\infty/c_\infty = 2.5$ . In this run with  $\Delta_{\mathcal{T}} = 1.8$  (see Fig. 4), the I-front is stable, although the shell is thinner than the critical value 0.05 ( $\Delta R_{\text{shell}}/R_{\text{IF}} \sim 0.02$ ). We attribute the stability of this run to the weak temperature increase across the I-front ( $\Delta_{\mathcal{T}} \sim 1$ ), also observed in the run with the same  $n_\infty$  and  $M_{\text{BH}}$  but with  $v_\infty/c_\infty = 2$  in Fig. 5. In runs with the same  $n_\infty$  and  $M_{\text{BH}}$  but  $\Delta_{\mathcal{T}} \approx 600$  due to  $T_\infty = 30 \text{ K}$ , the I-fronts are unstable if  $\Delta R_{\text{shell}}/R_{\text{IF}} \leq 0.05$  (Fig. 4), supporting our conjecture that  $\Delta_{\mathcal{T}}$  determines the strength of the imbalance between thermal and ram pressure in the presence of shell distortions, hence is an important parameter for the growth of the instability. From the simulation results, we infer that  $\Delta_{\mathcal{T}} \geq 3$  is a necessary condition for the existence of the instability.

The ionization parameter  $\xi$  and  $\Delta_{\mathcal{T}}$  (see Sec. 4.1) are proportional to  $L^{1/3} n_{\text{II}}^{1/3}$  (Eq. 27), and hence we can reformulate the condition  $\Delta_{\mathcal{T}} \geq 3$  as

$$L \geq (10^{37} \text{ erg/s}) \left( \frac{n_{\text{II}}}{10^4 \text{ cm}^{-3}} \right)^{-1}. \quad (31)$$

To derive this condition, we used  $L = 2 \times 10^{37} \text{ erg/s}$  for the runs with  $n_\infty = 10^4 \text{ cm}^{-3}$  (see Sec. 3) and  $n_{\text{II}} \approx 2n_\infty = 2 \times 10^4 \text{ cm}^{-3}$  with  $v_\infty$  around  $v_{\text{R}} \sim 2c_{\text{II}}$  (Eq. 7). In the RIAF

regime,  $\xi$  is also proportional to  $n_\infty M_{\text{BH}}$  (Eq. 28), and thus the above condition is equivalent to

$$n_\infty M_{\text{BH}} \geq 10^6 M_\odot \text{cm}^{-3}. \quad (32)$$

In addition, using Eqs. (7) and (16), we find  $d_r/R_{\text{IF}} \propto (M_{\text{BH}} n_\infty)^{-1}$ . Hence, the condition for the existence of unstable modes,  $d_r/R_{\text{IF}} < 1$ , is more strongly satisfied with increasing  $n_\infty M_{\text{BH}}$ . Although we have confirmed that  $d_r/R_{\text{IF}} < 1$  in our simulations with  $n_\infty M_{\text{BH}} \geq 10^5 M_\odot \text{cm}^{-3}$ , the relatively larger  $d_r/R_{\text{IF}}$  in the run with  $n_\infty = 10^3 \text{cm}^{-3}$ ,  $M_{\text{BH}} = 10^2 M_\odot$  and  $v_\infty/c_\infty = 2.5$  may contribute to suppressing the instability. Finally, we also note that the opacity to ionizing radiation of shell is also proportional to  $n_\infty M_{\text{BH}}$ , as shown in Eq. (26). Thus, the lower opacity and self-shielding of the shell in the cases with smaller  $n_\infty M_{\text{BH}}$  may also have a stabilizing effect. In summary, the parameter combination  $n_\infty M_{\text{BH}}$  controls the nature of the flow and the stability of I-front around moving BHs. As inferred from our simulation results, we regard the condition  $n_\infty M_{\text{BH}} \geq 10^6 M_\odot \text{cm}^{-3}$  as the second necessary condition for having unstable and fragmenting shells around moving BHs.

### 4.3 Region III: unstable R-type flows

For velocities  $v_\infty \gtrsim v_{\text{R}}$ , the dense shell disappears and the flow becomes R-type. For a range of velocities around the critical value, however, the transition between the D- and R-type flows is difficult to define because the I-front is not steady due to the instability. As a reference case for the R-type flow in the Region III in Figure 1, we perform the run with  $n_\infty = 10^5 \text{cm}^{-3}$ ,  $M_{\text{BH}} = 10^2 M_\odot$ ,  $T_\infty = 10^4 \text{K}$ , and  $v_\infty/c_\infty = 7$  and shows the snapshot at a time after the instability is fully developed and saturated in Figure 8. Unexpectedly, with respect to the results in PR13, we find that the R-type I-front is also unstable. Similarly to the case of the unstable D-type flow, in the non-linear regime, the instability strongly distorts the I-front and dense regions form at the receding gaps of the I-front. This type of instability was not observed in PR13, probably because the resolution at the I-front was not sufficiently high due to the logarithmic grid in the radial direction. By performing low-resolution simulations, we find that the instability disappears when the resolution near the I-front is below  $\Delta x/R_{\text{IF}} = 0.05$ . We would also like to emphasize again that the growth of instability is essentially a 3D process and cannot be fully captured by 2D simulations.

The unstable nature of weak R-type I-front has been known since the late 1960s. Newman & Axford (1967) studied the stability of the weak R-type I-front using linear analysis for a plane-parallel and infinitely-thin I-front. Newman & Axford (1967) explained the mechanism of instability as follows: the parts of the perturbed I-front getting displaced upstream, the relative flow velocity with respect to the I-front becomes higher; thus the density behind the I-front becomes smaller according to the jump condition for weak R-type I-front (see Eq. 1 with minus sign). Consequently, the absorption of ionizing photons by recombining neutral hydrogen is suppressed, leading to a further displacement upstream of the I-front. Vice versa for the perturbed I-front displaced in the downstream direction. The linear analysis showed that all modes are unstable irrespective of their wavelength  $\lambda$ , and the growth timescale becomes shorter at

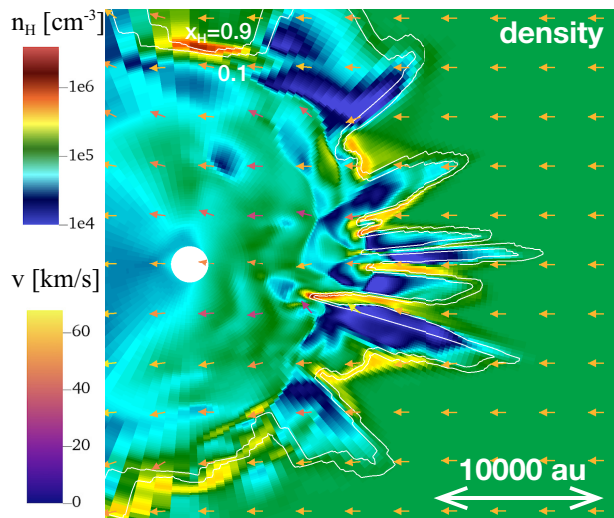


**Figure 8.** The same as Fig. 3 but for the run with  $n_\infty = 10^5 \text{cm}^{-3}$  and  $v_\infty/c_\infty = 7$  at a time after the instability is fully developed and saturated.

smaller wavelengths, until  $\lambda \simeq d_r$ , below which the growth time scale remains nearly constant. In less idealized conditions, however, we expect that the instability for small-scale modes may be suppressed by effects not included in the linear analysis, such as the finite thickness of the I-front and possible presence of magnetic fields (Axford 1964). For a mode with fixed  $\lambda$ , the growth time scale of the instability is nearly constant with the velocity  $v_1$ , but decreases at most by a factor of two as  $v_1$  approaches  $v_{\text{R}}$ . The growth time scale of the fastest modes is of the order of the recombination time scale  $t_{\text{rec}} = 1/n\pi\alpha_{\text{B}}$ .

While Newman & Axford (1967) showed that the weak R-type I-fronts are always unstable, they concluded that the growth of the instability was insignificant because the duration of the expanding R-type phase of an HII region is only about  $t_{\text{rec}}$ , and thus the instability does not have enough time to grow substantially. In the current case of moving BH, however, weak R-type I-fronts continue to exist for a much longer time, and thus there is enough time for the instability to grow until it becomes non-linear and saturates.

As shown in Fig. 8, the simulation results confirm the linear analysis expectations: in the runs with  $n_\infty = 10^5 \text{cm}^{-3}$ ,  $M_{\text{BH}} = 10^2 M_\odot$ , and  $v_\infty/c_\infty = 7$  and 10, the I-front is unstable. At lower ambient density, in the runs with  $n_\infty = 10^4 \text{cm}^{-3}$ ,  $M_{\text{BH}} = 10^2 M_\odot$ , and  $v_\infty/c_\infty = 4-10$ , we again observe the instability of the R-type flows. The distortion of I-front and the density contrast of the front fragments, however, becomes less significant than in the higher density runs. With an even weaker temperature jump, in the runs with  $n_\infty = 10^3 \text{cm}^{-3}$ ,  $M_{\text{BH}} = 10^2 M_\odot$ , and  $v_\infty/c_\infty = 3-10$ , the instability of the R-type flows becomes insignificant. We further confirm the requirement of large  $\Delta_{\text{T}}$  for the growth of I-front instabilities, by performing runs with  $\Delta_{\text{T}} \approx 600$ , assuming  $T_{\text{I}} = T_\infty = 30 \text{K}$  (X-ray preheating artificially suppressed). We find that the R-type I-front is unstable in the run with  $v_\infty = 4 c_s(T = 10^4 \text{K}) = 70 c_\infty$ . The instability, however, does not grow in the run with  $v_\infty = 7 c_s(T = 10^4 \text{K}) = 130 c_\infty$ . This case suggests that the instability may become weak if the Mach number is very large, although this case is unlikely to

be realized in nature because we expect that  $T_1 \sim 10^4$  K due to X-ray preheating, especially for R-type flows in which a shell optically thick to X-rays is not present. In the runs with  $n_\infty = 10^4 \text{ cm}^{-3}$ ,  $M_{\text{BH}} = 10^3 M_\odot$ , and  $v_\infty/c_\infty = 7$  and 10, the front is strongly unstable similarly as in the reference run, because the temperature profiles are identical in these two cases that have the same  $n_\infty M_{\text{BH}}$ .

In the same way as the thin-shell instability of the D-type flow, the steep temperature jump is a necessary condition in order for the instability to grow. As mentioned above, the instability is driven by the variation of the density behind the I-front as the flow velocity varies behind the perturbed front. The density behind the front depends on the flow velocity more weakly as the ratio  $\Delta_T$  approaches unity (Eq. 1). Therefore, a steeper temperature jump enhances the strength of the instability. The condition for a steep enough temperature jump is to have a large ionization parameter  $\xi$  just behind the I-front. In our constant luminosity simulations of the D-type and R-type flows, we assume a constant luminosity  $L$  at the value  $v_\infty = 4 c_\infty$ , irrespective of the actual value of  $v_\infty$  in the runs (see Sec. 3). This is a good approximation for unstable D-type flows in the range of  $v_{\text{crit}} < v_\infty < v_{\text{R}}$ , as well as for R-type flows with  $v_\infty \gtrsim v_{\text{R}}$ , because for this velocity range the luminosity does not change significantly as a function of  $v_\infty$ . With this assumption we have found that the I-front is unstable owing to large enough  $\xi$  if  $n_\infty M_{\text{BH}} \geq 10^6 M_\odot \text{ cm}^{-3}$ .

However, for the R-type flows with large  $v_\infty$  (*i.e.*, when  $v_\infty \gg v_{\text{R}}$ ), the reduction of  $L$  from the value assumed in our constant luminosity simulations can be significant. Therefore, here we derive a more accurate instability criterion allowing a realistic dependence of  $L$  on  $v_\infty$ . In the high-velocity limit ( $v_\infty \gg v_{\text{R}}$ ), Eqs. (8) and (10)–(12), give  $L \propto M_{\text{BH}}^3 n_\infty^2 v_\infty^{-6}$ , and thus Eq. (27) yields  $\xi \propto L^{1/3} n_{\text{II}}^{1/3} \propto M_{\text{BH}} n_\infty v_\infty^{-2}$ . From Eqs. (8)–(12), the actual value of  $L$  for  $v_\infty = 100 \text{ km/s}$  is about  $10^3$  times smaller than the assumed constant value of  $L$  for  $v_\infty = 4 c_\infty$ . Therefore, by rewriting the condition of  $\xi$  larger than the critical value corresponding to  $n_\infty M_{\text{BH}} = 10^6 M_\odot \text{ cm}^{-3}$  and  $L$  for  $v_\infty = 4 c_\infty$  with Eq. (27), we obtain the instability condition for R-type I-fronts:

$$n_\infty M_{\text{BH}} \geq (10^7 M_\odot \text{ cm}^{-3}) \left( \frac{v_\infty}{100 \text{ km/s}} \right)^2 \quad (v_\infty \gg v_{\text{R}}). \quad (33)$$

We have confirmed the validity of this condition by performing additional runs with  $n_\infty = 10^4 \text{ cm}^{-3}$ ,  $v_\infty = 13 c_\infty \approx 100 \text{ km/s}$ , and two different masses:  $M_{\text{BH}} = 10^2$  and  $10^3 M_\odot$ , for which we determine  $L$  including the  $v_\infty$  dependence. The I-front in the run with the smaller mass is stable, while in the other run is unstable, confirming the validity of our stability criteria.

## 5 DISCUSSIONS

### 5.1 Conditions for Instability

In Sec. 4, we have observed that I-fronts around moving BHs can be either stable or unstable, depending on the parameters of the system. Below, we will summarize and discuss the conditions for the instability based on our results.

We have found that a sufficiently large temperature

jump,  $\Delta_T > 3$ , across the I-front is a necessary condition for the instability. This first condition is satisfied if  $L \geq 10^{37} \text{ erg/s} (m_{\text{II}}/10^4 \text{ cm}^{-3})^{-1}$ , which is equivalent to  $n_\infty M_{\text{BH}} \geq 10^6 M_\odot \text{ cm}^{-3}$  for D-type flows (and low-velocity R-type flows) and  $n_\infty M_{\text{BH}} \geq 10^7 M_\odot \text{ cm}^{-3} (v_\infty/100 \text{ km/s})^2$  for high-velocity R-type flows (with  $v_\infty \gg v_{\text{R}}$ ). This condition is also satisfied if  $T_1 \lesssim 5000 \text{ K}$  (given that  $T_{\text{II}}$  has a lower floor  $\sim 1.5 \times 10^4 \text{ K}$  for zero-metallicity gas). However, even if the ambient temperature  $T_\infty$  is cold, the incident flow is heated to a temperature  $T_1 \sim 10^4 \text{ K}$  by X-ray pre-heating before reaching either the shock (for D-type flows) or the I-front (for R-type flows), unless the dense shell preceding D-type fronts is optically thick to X-rays (see Appendix A2).

In order for the instability to exist, the flow needs to be either D-type with a sufficiently thin shell ( $\Delta R_{\text{shell}}/R_{\text{IF}} < 0.05$ ) or an R-type flow. This requirement yields the second condition for the instability:  $v_\infty/c_\infty \geq 3-4$ , or  $v_\infty \geq 20-30 \text{ km/s}$ , with the minimum value slightly depending on the temperature profile in the HII region.

Now, let us discuss the (in)stability of the I-fronts around actual moving BHs, by applying the above two conditions to astrophysical situations. The first condition of  $n_\infty M_{\text{BH}}$  is rarely satisfied if we consider stellar-mass BHs with  $M_{\text{BH}} < 10^2 M_\odot$  moving in local galaxies because  $n_\infty \geq 10^4 \text{ cm}^{-3}$  required for the instability is significantly higher than the mean density of typical molecular clouds ( $\sim 10^2 \text{ cm}^{-3}$ ). However, this does not exclude the occurrence of the instability. IMBHs with  $M_{\text{BH}} = 10^{5-6} M_\odot$  are expected to exhibit the front instability even as moving in the cold and warm atomic phases of the interstellar medium  $\sim 1-10 \text{ cm}^{-3}$ . Moreover, the instability is expected to be important in high-redshift galaxies as their interstellar medium and molecular clouds have mean densities higher than that of local galaxies.

The second condition of  $v_\infty$  is easily satisfied. If we consider BHs moving at about the circular velocity of the host galaxies ( $\sim 100 \text{ km/s}$ ), the velocity of such BHs is larger than the value needed for the instability ( $20-30 \text{ km/s}$ ), as well as the critical velocity for the D- and R-type transition ( $v_{\text{R}} \sim 30-55 \text{ km/s}$  depending on the temperature profile). Therefore, the R-type flows around these BHs are unstable if the first condition of  $n_\infty M_{\text{BH}}$  is satisfied. If the dynamical friction by stars and gas works effectively and reduces the relative velocity between the gas and the BHs, the flows first become D-type with possibly-unstable thin shells and then D-type with stable thick shells. The effect of the gas dynamical friction, however, can be weakened or even reversed due to the gravitational attraction by the shells of the D-type flows (Park & Bogdanović 2017; Toyouchi et al. 2020).

### 5.2 Accretion and Radiation Bursts

The instability of the I-fronts observed in our simulations may lead to the accretion and radiation bursts. The dense clumps forming as a result of the instability possibly fall directly into the BHL radius and cause accretion bursts (see PR13). The associated radiation bursts would affect the gas dynamics on the scale of the I-front, producing periodic break up the I-front. The interaction of the gas dynamics and the time-varying radiation flux produces a complicated feedback loop, which will be addressed in future work.

The accretion and radiation bursts can have various

astrophysical consequences. The burst-mode accretion may enhance the time-averaged accretion rate and alleviate the problem of the inefficient seed IMBH growth in models of SMBH formation (see, e.g., Sugimura et al. 2018). Even if the time-averaged accretion rate is not modified, the accretion bursts can increase the total amount of X-ray emission because the radiative efficiency is higher for a higher accretion rate in the RIAF regime. The modified X-ray emission can affect the star-formation history of the Universe through the build-up of an X-ray background (see, e.g., Ricotti 2016). Finally, the radiation bursts may temporarily enhance the luminosity of moving IMBHs not detectable without bursts to the range of the ultraluminous X-ray sources (ULXs; see, e.g., Miller & Colbert 2004, for review), opening the way to the observation of such IMBHs in nearby galaxies. We will discuss in more detail this last point in the next section.

### 5.3 X-rays from Moving IMBHs: Observational Implications

Although more work needs to be done to correctly link the I-front instability to the change of BH accretion rate and luminosity, here we briefly discuss possible observational signatures and tests of our model. We first discuss observations of steady radiation from moving BHs and then make qualitative prediction considering the possibility of luminosity bursts associated with the I-front instability.

Currently, observations have sufficient sensitivity to detect X-ray (and possibly radio) emission from moving IMBHs accreting from molecular clouds in the interstellar medium (e.g., Ipser & Price 1977; Fujita et al. 1998; Gaggero et al. 2017; Ioka et al. 2017; Matsumoto et al. 2018; Manshanden et al. 2019). There are two promising sites for finding such IMBHs. The first is the Galactic center, where the gas density is high and IMBHs may be more concentrated within the Galaxy. At the Galactic center, the steady accretion model in Sec. 2.1 and Appendix A predicts that IMBHs with  $M_{\text{BH}} \gtrsim 10^2 M_{\odot} (n_{\text{H}}/10^2 \text{ cm}^{-3})^{-2/3}$  have X-ray luminosity  $L_{\text{X}} > 4 \times 10^{32} \text{ erg/s}$ , which is the luminosity limit of the *Chandra* X-ray source catalog (Muno et al. 2009). For this rough estimate we have assumed that IMBH velocity is  $\sim 40 \text{ km/s}$ , hence the luminosity is near the peak value, and that the X-ray luminosity is 30% of the bolometric luminosity (Manshanden et al. 2019). The second strategy to find IMBHs is in dwarf galaxies, because they are gas rich and because of the larger number of IMBHs with velocities near  $40 \text{ km/s}$  (due to the lower virial velocity of dwarf galaxies with respect to the Milky Way). *Chandra* provided X-ray source catalog for sources with  $L_{\text{X}} > 4 \times 10^{35} \text{ erg/s} (d_{\text{L}}/2 \text{ Mpc})^2$  in the COSMOS field (Civano et al. 2016), and thus IMBHs with masses  $M_{\text{BH}} \gtrsim 10^3 M_{\odot} (n_{\text{H}}/10^2 \text{ cm}^{-3})^{-2/3} (d_{\text{L}}/2 \text{ Mpc})^{2/3}$  are detectable if we make the same assumptions as above.

The luminosity bursts associated with the I-front instability are expected to be significantly brighter than the steady state luminosity, but short lived. Therefore, accounting for these luminosity bursts, there will be a small fraction (due to the short duty cycle of the burst) of the accreting IMBH population with higher luminosity. As a result, the X-ray luminosity function may show a small (in term of number of object) high-luminosity component above the critical luminosity for the instability,  $\sim 10^{37} \text{ erg/s} (n_{\text{H}}/10^4 \text{ cm}^{-3})$  (Eq. 31). While such luminous objects have already been

strongly constrained near the Galactic center, the precision of the luminosity function in dwarf galaxies will be greatly improved in the future. For example, *Athena* plans an X-ray survey that increases the area by one order of magnitude and sensitivity by two orders of magnitude with respect to the current observational limits (Aird et al. 2013). Detailed modeling of the X-ray luminosity function in the Galactic center and nearby dwarfs may provide a test of our model for the instability of the I-front. However, in order to estimate the increase of luminosity during the bursts due to fragment of the shell falling into the IMBH, we need full 3D simulations of moving BHs with gravity and radiative feedback.

## 6 SUMMARY

In this paper, we have studied the structure and instability of the ionization fronts (I-fronts) around moving black holes (BHs), by performing a series of 3D radiation hydrodynamics simulations with high-resolution around the I-front, and assuming a constant luminosity from the BH. To provide a physical interpretation of the structures observed in the simulations, we have developed an analytical model of the bow-shock preceding the D-type I-fronts and studied the conditions for their instability.

The I-front makes a transition from D- to R-type as we increase the BH velocity  $v_{\infty}$ , and the D-type front becomes unstable for velocities above a critical value  $v_{\infty} \approx 20\text{--}30 \text{ km/s}$ , when the ratio of the shell thickness to the size of the I-front is smaller than 0.05. The R-type flow is instead always unstable irrespective of  $v_{\infty}$ , with the possible exception of very large Mach numbers ( $> 100$ ). However, the instability grows only if  $n_{\text{H}} M_{\text{BH}} \gtrsim 10^6 M_{\odot} \text{ cm}^{-3}$ , for which the ionization parameter at the I-front and therefore the temperature jump  $\Delta_{\mathcal{T}} \equiv T_{\text{II}}/T_{\text{I}}$  is larger than a critical value ( $\Delta_{\mathcal{T}} \geq 3$ ). Although this last condition is rarely satisfied for stellar-mass BHs moving in local molecular clouds, we expect that intermediate-mass BHs (IMBHs) moving in the denser interstellar medium (ISM) of galaxies in the early Universe would exhibit I-front instabilities, which may lead to accretion and radiation bursts. Such bursts would increase the IMBH growth rate, contribute to the build-up of the X-ray background, and improve the observability of IMBHs accreting from molecular clouds.

This paper is a first step to better understand the entire process of gas accretion onto moving IMBHs, including the possible accretion and radiation bursts due to the instability of the I-front.

## ACKNOWLEDGEMENTS

The authors thank Takashi Hosokawa, Daisuke Toyouchi, and Hidenobu Yajima for fruitful discussions and comments. K.S. appreciates the support by the Fellowship of the Japan Society for the Promotion of Science for Research Abroad. M.R. acknowledges the support by NASA grant 80NSSC18K0527. The numerical simulations were performed on the Cray XC50 at CfCA of the National Astronomical Observatory of Japan, as well as on the computer

cluster, Draco, at Frontier Research Institute for Interdisciplinary Sciences of Tohoku University, and on the Cray XC40 at Yukawa Institute for Theoretical Physics in Kyoto University. The authors also acknowledge the University of Maryland supercomputing resources (<http://hpcc.umd.edu>) made available for conducting the research reported in this paper. We thank the anonymous reviewer for helping improve the quality of this paper.

## REFERENCES

- Aird J., et al., 2013, arXiv e-prints, p. arXiv:1306.2325  
 Axford W. I., 1964, ApJ, 140, 112  
 Civano F., et al., 2016, ApJ, 819, 62  
 Ferland G. J., Peterson B. M., Horne K., Welsh W. F., Nahar S. N., 1992, ApJ, 387, 95  
 Fujita Y., Inoue S., Nakamura T., Manmoto T., Nakamura K. E., 1998, ApJ, 495, L85  
 Gaggero D., Bertone G., Calore F., Connors R. M. T., Lovell M., Markoff S., Storm E., 2017, Phys. Rev. Lett., 118, 241101  
 Garcia-Segura G., Franco J., 1996, ApJ, 469, 171  
 Giuliani Jr. J. L., 1979, ApJ, 233, 280  
 Hosokawa T., Hirano S., Kuiper R., Yorke H. W., Omukai K., Yoshida N., 2016, ApJ, 824, 119  
 Inayoshi K., Haiman Z., Ostriker J. P., 2016, MNRAS, 459, 3738  
 Inayoshi K., Visbal E., Haiman Z., 2019, arXiv e-prints, p. arXiv:1911.05791  
 Ioka K., Matsumoto T., Teraki Y., Kashiyama K., Murase K., 2017, MNRAS, 470, 3332  
 Ipser J. R., Price R. H., 1977, ApJ, 216, 578  
 Keshet U., Naor Y., 2016, ApJ, 830, 147  
 Kuiper R., Klessen R. S., 2013, A&A, 555, A7  
 Kuiper R., Klahr H., Dullemond C., Kley W., Henning T., 2010a, A&A, 511, A81  
 Kuiper R., Klahr H., Beuther H., Henning T., 2010b, ApJ, 722, 1556  
 Kuiper R., Klahr H., Beuther H., Henning T., 2011, ApJ, 732, 20  
 Manshanden J., Gaggero D., Bertone G., Connors R. M. T., Ricotti M., 2019, J. Cosmology Astropart. Phys., 2019, 026  
 Matsumoto T., Teraki Y., Ioka K., 2018, MNRAS, 475, 1251  
 Mignone A., Bodo G., Massaglia S., Matsakos T., Tesileanu O., Zanni C., Ferrari A., 2007, ApJS, 170, 228  
 Miller M. C., Colbert E. J. M., 2004, International Journal of Modern Physics D, 13, 1  
 Milosavljević M., Couch S. M., Bromm V., 2009a, ApJ, 696, L146  
 Milosavljević M., Bromm V., Couch S. M., Oh S. P., 2009b, ApJ, 698, 766  
 Muno M. P., et al., 2009, ApJS, 181, 110  
 Narayan R., Yi I., 1994, ApJ, 428, L13  
 Newman R. C., Axford W. I., 1967, ApJ, 149, 571  
 Park K., Bogdanović T., 2017, ApJ, 838, 103  
 Park K., Ricotti M., 2011, ApJ, 739, 2  
 Park K., Ricotti M., 2012, ApJ, 747, 9  
 Park K., Ricotti M., 2013, ApJ, 767, 163  
 Ricotti M., 2016, MNRAS, 462, 601  
 Sugimura K., Hosokawa T., Yajima H., Omukai K., 2017, MNRAS, 469, 62  
 Sugimura K., Hosokawa T., Yajima H., Inayoshi K., Omukai K., 2018, MNRAS, 478, 3961  
 Takeo E., Inayoshi K., Ohsuga K., Takahashi H. R., Mineshige S., 2018, MNRAS, 476, 673  
 Toyouchi D., Hosokawa T., Sugimura K., Nakatani R., Kuiper R., 2019, MNRAS, 483, 2031  
 Toyouchi D., Hosokawa T., Sugimura K., Kuiper R., 2020, arXiv e-prints, p. arXiv:2002.08017  
 Vishniac E. T., 1983, ApJ, 274, 152  
 Volonteri M., 2012, Science, 337, 544  
 Whalen D. J., Norman M. L., 2008a, ApJ, 672, 287  
 Whalen D., Norman M. L., 2008b, ApJ, 673, 664  
 Yajima H., Ricotti M., Park K., Sugimura K., 2017, ApJ, 846, 3  
 Yalinewich A., Sari R., 2016, ApJ, 826, 177

## APPENDIX A: REVISED ACCRETION RATE FORMULA INCLUDING X-RAY PREHEATING AND EXTENSION TO SUBSONIC VELOCITIES

Here, we provide an accretion rate formula that includes X-ray preheating and extension to subsonic velocities, by revising the Park & Ricotti model described in Sec. 2.

### A1 Subsonic case

Let us begin by describing the subsonic case with  $v_\infty < c_I$ . In this case, not only is the shocked shell of the D-type flow replaced with a gradual density enhancement, but also the effect of the vertical motion relative to the parallel motion becomes significant and the approximation of the 1D plane-parallel flow breaks down as the velocity decreases. Therefore, we interpolate the accretion rates at  $v_\infty = c_I$  and 0, instead of modelling the accretion rate with the 1D plane-parallel model.

In the limit of  $v_\infty = 0$ , the system becomes the well-known spherical symmetric case, in which the accretion is episodic, but the average accretion rate is approximately given by the Bondi accretion rate for the ionized region (Milosavljević et al. 2009a; Park & Ricotti 2011). With the assumption of pressure equilibrium between the inner ionized and outer neutral gas,  $\rho_\infty c_I^2 = \rho_{II} c_{II}^2$ , the accretion rate is given by  $\dot{M}_{v=0} = 4\pi\lambda_B G^2 M_{BH}^2 \rho_\infty c_I^2 / c_{II}^5$ , where we set the coefficient  $\lambda_B = 1$  ( $\lambda_B = 1.12$  for the isothermal gas).

To make an interpolation between  $v_\infty = 0$  and  $c_I$ , we assume that the velocity inside the ionized bubble scales linearly with  $v_\infty$  as  $v_{II} \approx c_{II} (v_\infty / c_I)$  and that the total pressure is conserved along the flow, which gives the density  $\rho_{II} = \rho_\infty (c_I^2 + v_\infty^2) / (c_{II}^2 + v_{II}^2)$ . Then, the formula for the BHL accretion rate (the second expression in Eq. 8) yields the accretion rate for  $0 \leq v_\infty < c_I$ ,

$$\dot{M}_{\text{sub-soinc}} = \frac{4\pi G^2 M_{BH}^2 \rho_\infty (c_I^2 + v_\infty^2)}{c_{II}^5} \left( 1 + \left( \frac{v_\infty}{c_I} \right)^2 \right)^{-\frac{5}{2}}, \quad (\text{A1})$$

which converges to  $\dot{M}_{v=0}$  at  $v = 0$  and  $\dot{M}_D$  (Eq. 9) at  $v = c_I$ , as expected. In Fig. A1, we show  $\dot{M}$  given by Eqs. (8) and (A1) for  $0 \leq v_\infty \leq 80$  km/s.

### A2 Case with X-ray preheating

Next, let us consider the case with X-ray preheating. Although we assume the constant neutral gas temperature  $T_I$  in Sec. 2.1 and Appendix. A1, the temperature far from the BH can be lowered by the metal or molecular cooling, as studied in Toyouchi et al. (2020). In their simulations with metal cooling, the temperature of incident gas gradually increases as the gas approaches the BH due to the heating by the X-rays leaking out of the I-front (*i.e.*, X-ray preheating). Here, we assume that even if the ambient temperature  $T_\infty$  is cold, the incident flow is heated by X-rays to a temperature



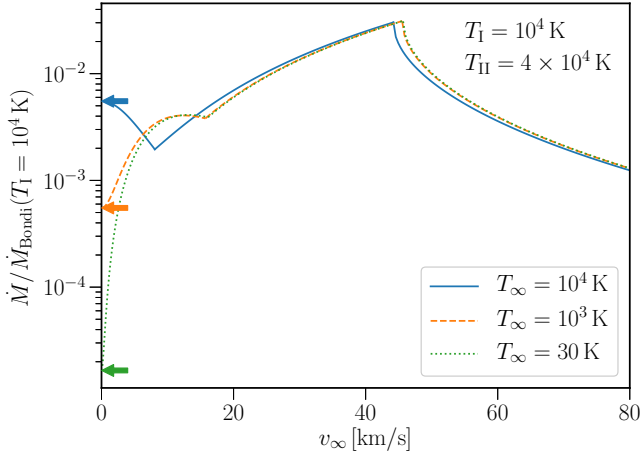


**Figure A1.** Same as Fig. 1 but for the accretion rate normalized by the Bondi rate for neutral gas with  $T_I = 10^4$  K,  $\dot{M}_{\text{Bondi}} = 4\pi G^2 M_{\text{BH}}^2 / c_I^3$ , for the velocity range including the subsonic case. We here plot the accretion rate for the case with the constant temperature outside the I-front given by Eqs. (8) and (A1) and those for the case with X-ray preheating given by Eq. (A3). The temperatures of ambient gas are  $T_\infty = 10^4$  K (solid),  $10^3$  K (dashed), and 30 K (dotted), while that of the ionized region is  $T_{\text{II}} = 4 \times 10^4$  K and that of the neutral region after X-ray preheating is  $T_I = 10^4$  K, if it exists. The arrows represent the values for the static BHs.

$T_I \sim 10^4$  K, which is determined by the steep temperature dependence of the Ly $\alpha$  cooling, before reaching either the shock (in D-type flows) or the I-front (in R-type flows). In the following, we adopt subscripts  $\infty$  and I for quantities before and after the X-ray preheating, respectively. The analytical model in Sec. 2.1 and Appendix A1 is still valid if we assume as boundary conditions at infinity the values after the X-ray preheating. Note that X-ray preheating may be suppressed due to the attenuation of X-rays by gas or dust grains in the dense shell preceding the D-type I-fronts. Using the effective cross-section for Compton scattering and dust attenuation per hydrogen atom  $\sigma_{\text{eff}} = \sigma_T (1 + 710 (Z/Z_\odot))$  (Yajima et al. 2017) and the column density of the shell  $\Delta N_{\text{shell}}$  given by Eq. (26), we can give a rough estimate of the optical depth to X-rays of the shell:

$$\tau_X = \Delta N_{\text{shell}} \sigma_{\text{eff}} \quad (\text{A2})$$

$$= 2 \times 10^{-3} \left( \frac{n_\infty M_{\text{BH}}}{10^6 M_\odot \text{cm}^{-3}} \right) \left( 1 + 710 \left( \frac{Z}{Z_\odot} \right) \right) \left( 1 - \frac{v_\infty}{v_R} \right).$$

The equation above suggests that, assuming a relatively hard X-ray spectrum, X-ray preheating can be suppressed in gas at solar or supersolar metallicities, but is always effective in gas of primordial composition. A soft X-rays spectrum could be more easily attenuated by photoelectric absorption by helium and metal ions, perhaps suppressing pre-heating even at relatively low gas metallicities. We plan to investigate the effect of X-ray preheating in more detail in future works.

In response to the temperature variation, the density and velocity also change from their ambient values  $\rho_\infty$  and  $v_\infty$ . For the supersonic part of the flow, we consider a quasi-1D plane-parallel model similar to that for the R-type flows in Sec. 2.1. From mass and momentum conservation, we obtain the analogue of the I-front jump condition given by Eq. (1): the density  $\rho_I$  and velocity  $v_I$  after the X-ray pre-

heating are given as  $\rho_I/\rho_\infty = v_\infty/v_I = \Delta^{(-)}(v_\infty, c_\infty, c_I)$  if  $v_\infty > v_R(c_\infty, c_I)$ , where  $v_R(c_\infty, c_I) \approx 2c_I$  for  $c_\infty \ll c_I$ . If  $v_\infty < v_R(c_\infty, c_I)$ , however, a shock may form in the pre-heating transition region because the above jump conditions give unphysical (imaginary) values, as in the case of the D-type flows in Sec. 2.1. In such a case, we again interpolate the results for  $v_\infty = 0$  and  $v_R(c_\infty, c_I)$ , as the quasi-1D plane-parallel approximation is not appropriate for the post-shocked subsonic flows. Since  $v_I$  is equal to 0 if  $v_\infty = 0$  and  $c_I$  if  $v_\infty = v_R(c_\infty, c_I)$ , we assume  $v_I = c_I v_\infty / v_R(c_\infty, c_I)$ . We obtain the density  $\rho_I = \rho_\infty (c_\infty^2 + v_\infty^2) / (c_I^2 + v_I^2)$  from the conservation of the total pressure, as assumed in Sec. 2.1.

Finally, we obtain the accretion rate  $\dot{M}$  for the case with X-ray preheating, using the above expressions for  $\rho_I$  and  $v_I$  after the temperature reaches  $T_I$ . From the formula for  $\dot{M}$  for the case with fixed neutral-gas temperature (Eqs. 8 and A1), we obtain

$$\dot{M} = \begin{cases} \dot{M}_{\text{sub-sonic}} & 0 \leq v_\infty < v_R(c_\infty, c_I) \\ \dot{M}_D & v_R(c_\infty, c_I) < v_\infty < v_R(c_I, c_{\text{II}}) \\ \dot{M}_R & v_R(c_I, c_{\text{II}}) < v_\infty \end{cases}, \quad (\text{A3})$$

with

$$\dot{M}_{\text{sub-sonic}} = \frac{4\pi G^2 M_{\text{BH}}^2 \rho_\infty (c_\infty^2 + v_\infty^2)}{c_{\text{II}}^5} \left( 1 + \left( \frac{v_\infty}{v_R(c_\infty, c_I)} \right)^2 \right)^{-\frac{5}{2}}, \quad (\text{A4})$$

$$\dot{M}_D = \frac{\pi G^2 M_{\text{BH}}^2 \rho_\infty (v_\infty^2 + c_\infty^2)}{\sqrt{2} c_{\text{II}}^5}, \quad (\text{A5})$$

and

$$\dot{M}_R = \frac{4\pi G^2 M_{\text{BH}}^2 \rho_\infty \Delta^{(-)}(v_\infty, c_\infty, c_{\text{II}})}{\left( c_{\text{II}}^2 + \left( \frac{v_\infty}{\Delta^{(-)}(v_\infty, c_\infty, c_{\text{II}})} \right)^2 \right)^{\frac{3}{2}}}. \quad (\text{A6})$$

In Fig. A1, we plot  $\dot{M}$  for the case with X-ray preheating, setting  $T_\infty = 30$  and  $10^3$  K and  $T_I = 10^4$  K. In Eqs. (A5) and (A6), we have simplified the expressions using the conservation of the total pressure and the mass flux along the flow. Note that the velocities at which the expression for  $\dot{M}$  changes from  $\dot{M}_{\text{sub-sonic}}$  to  $\dot{M}_D$  and from  $\dot{M}_D$  to  $\dot{M}_R$  are  $v_R(c_\infty, c_I) \approx 2c_I$  ( $c_\infty \ll c_I$ ) and  $v_R(c_I, c_{\text{II}}) \approx 2c_{\text{II}}$  ( $c_I \ll c_{\text{II}}$ ), respectively. The accretion rate converges to the ordinary BHL value for  $v_\infty \gg 2c_{\text{II}}$ .

This paper has been typeset from a  $\text{\TeX}/\text{\LaTeX}$  file prepared by the author.